Mechanisms of Dominant Electrophysiological Features of Four Subtypes of Layer 1 Interneurons

John Hongyu Meng [1], Benjamin Schuman [2], Bernardo Rudy [2,3], Xiao-Jing Wang [1,*]

1 Center for Neural Science, New York University, New York, NY, 10003, USA
2 Neuroscience Institute, Department of Neuroscience and Physiology, New York University, New York, NY 10016, USA
3 Department of Anesthesiology, Perioperative Care, and Pain Medicine, New York University, New York, NY 10016, USA

*** xjwang@nyu.edu**

Abstract

Neocortical Layer 1 (L1) consists of GABAergic interneurons (INs) and receives extensive long-range "top-down" projections, but L1 INs remain poorly understood. In this work, we systematically examined the distinct dominant electrophysiological features for four unique IN subtypes in L1 that were previously identified: Canopy cells show an irregular firing pattern near rheobase; Neurogliaform cells (NGFCs) are late-spiking, and their firing rate accelerates during current injections; cells with strong expression of the $\alpha 7$ nicotinic receptor ($\alpha 7$ cells), display initial (rebound) bursting; vasoactive intestinal peptide (VIP) expressing cells exhibit high input resistance, strong adaptation, and irregular firing. Computational modelling revealed that these neurophysiological diverse features could be explained by an extended exponential-integrate-and-fire neuron model with varying contributions of a slowly inactivating K^+ channel (SIK), a T-type Ca^{2+} channel, and a spike-triggered Ca^{2+}-dependent K^+ channel. In particular, we show that irregular firing results from square-wave bursting through a fast-slow analysis. Furthermore, we demonstrate that irregular firing is frequently observed in VIP cells due to the interaction between strong adaptation and a SIK channel. The reported findings of single neuron dynamics should be incorporated to elucidate how different L1 cell types contribute to the integration of top-down signaling and local processes.

Introduction

Neocortical Layer 1, the most superficial layer of the cerebral cortex, is the main target of extensive "top-down" information conveyed by long-range inputs from other cortical regions and subcortical structures ([4], [11], [8], [26]). The integration of these inputs into local processing is thought to be mediated by a population of GABAergic inhibitory interneurons (INs) residing in L1 in addition to INs in deeper layers with dendrites or axons in L1. ([16], [8], [26]). To date, modeling studies have mostly neglected L1 INs in computational neuroscience. However, in order to study the impact of long-range inputs on cortical functions, a detailed understanding of local L1 circuitry is inevitable ([26]).

To dissect this process, L1 INs have been classified into different subtypes ([27]). Not limited to the L1, a classification system considering the definitive features that

differentiate IN populations such as gene expression, electrophysiological properties, and morphology is necessary to study the role of each IN subtype in cortical circuits ([34]). Essential findings have been achieved by tagging IN subtypes through genetic strategies ([34]), or exploiting the advantages of the Patch-seq technique to glean electrophysiologic and transcriptomic information from the same cell ([14], [25]). In a previous study, we identified four unique populations of INs with somas in L1, each with a distinct molecular profile, morphology, electrophysiology, and connectivity. These four types were Canopy cells, Neurogliaform cells (NGFCs), cells with high levels of the $\alpha 7$ nicotinic receptor ($\alpha 7$ cells), and vasoactive intestinal peptide (VIP) expressing cells ([27]).

However, models *in silico* of the functional properties of these cells are still lacking, which hinders the incorporation of these specialized L1 IN subtypes into circuit models. Models of single neurons have proved to be important for understanding the complex behavior and function of neuronal circuits ([33], [19]). From recent data ([15], [27], [12], [22]), it is of particular interest to understand the irregular firing pattern, which among INs is mostly observed in VIP cells ([34]). Irregular firing was a term initially used to describe the unpredictable firing pattern from trial to trial in response to the same depolarizing current injections, a unique feature observed in cells co-expressing VIP and calretinin from sensory-motor cortex of rats ([3]), and a subgroup of cannabinoid receptor-1 (CB_1) positive INs in the somatosensory cortex of mice ([10]). In addition, these cells have a high coefficient of variation of the ISI (CV ISI) and small subthreshold oscillations between spikes. Previously, one modeling study suggested the irregular firing arose from the noise-introduced transition between bistable states ([31]), which required fast activation kinetics of K^+ channels. In contrast, another study proposed that the subthreshold oscillation that enabled gamma resonances was strongly dependent on the slow inactivation of a Kv1 current ([28]). These hypotheses are worth a re-evaluation in our L1 dataset.

In this study, we identify salient electrophysiological features, irregularity (IR), acceleration (Acc) of firing rates, initial-bursting (IB), and adaptation (Adap) of firing rates within our L1 IN dataset, and further systematically examine the distribution of these features across the previously identified subtypes. We find Canopy cells show an irregular firing pattern near rheobase; NGFCs are late-spiking, and their firing rate accelerates during current injections; $\alpha 7$ cells display initial bursting; and VIP cells exhibit high input resistance, strong adaptation, and irregular firing. We then construct generic exponential integrate-and-fire (EIF) models for each IN subtype. We first show that a model with a slowly inactivating K^+ (SIK) channel can reproduce the irregular firing observed in Canopy cells through the mechanism of square-wave bursting ([24], [35], [23]). Second, by decreasing the conductance of the SIK channel, we reproduce the late-spiking and acceleration of NGFCs. Third, the initial bursting of $\alpha 7$ cells is reproduced by including a T-type calcium channel.

VIP cells in L1 have heterogeneous firing patterns, such as irregular firing, initial bursting, and strong adaptation in the firing rate. We first reproduce all these features in a generic VIP cell model that includes a SIK channel, a T-type Ca^{2+} channel, and a spike-triggered Ca^{2+}-dependent K^+ channel. A similar slow-fast analysis shows that irregularity in VIP cells has the same origin as in Canopy cells, which is square-wave bursting. Furthermore, we compare the heterogeneous firing patterns reproduced by varying parameters and conclude that irregular firing is more frequently observed in VIP cells due to the interaction between strong adaptation and the SIK channel.

In summary, the dominant electrophysiological features of the four L1 IN subtypes are analyzed and further reproduced in computational models, that explain the mechanisms underlying each subtype's electrophysiological properties. Also, we reveal that the co-existence of strong adaptation and SIK in the VIP cells leads to irregularity,

which is more frequently observed in the VIP cells ([34]). Lastly, the analysis we develop in this study will likely facilitate the classification of other neuronal cell types throughout the brain.

A sample data and the developed toolbox during this project are fully available online upon acceptance. The models in this study will be uploaded to the ModelDB upon acceptance. The full dataset is available upon request.

Results

Identifying dominant electrophysiological features of L1 interneuron subtypes

Previously, we separated the L1 IN population into Canopy cells, NGFCs, $\alpha 7$ cells, and VIP cells based on a combination of genetic markers, morphology, and basic electrophysiological features such as input resistance, sag, and latency to 1st spike ([27]). Here, we systematically studied more sophisticated electrophysiological features based on the analysis of all the sweeps in our dataset. We first identified four features of interest in this L1 dataset (figure 1A). Namely, irregular firing behavior (IR), acceleration of the firing rate (Acc), initial bursting (IB), and adaptation (Adap) of the firing rate.

Next, we set quantitative criteria to determine whether each cell shows these four features. Traditionally, irregularity is used to describe a unique unpredictable firing pattern ([10]). This can be further reflected in the abrupt change of the inter-spike intervals (ISI) (figure 1A1). To quantify it, we define an IR score of a pair of neighboring ISIs as one minus the ratio of the smaller ISI and the larger ISI. If one cell has at least three pairs of ISIs during the last $500ms$ of the the depolarizing pulse that have an IR score bigger than the threshold of 0.4, we consider the cell as having an IR feature. We only use the last $500ms$ to avoid the potential false-positive cases because cells with strong adap or IB can change firing rate rapidly at the onset of the injection current period. We also define a looser criterion for having an IR2 feature, i.e., if a cell does not display an IR feature but has at least one pair of ISIs during the latter $800ms$. If a cell with an IR2 feature may have an IR feature if the recordings were done with finer current steps, but it may not if the ISI pairs with large IR scores are purely introduced by noise. IR is widely observed in L1 INs except NGFCs (figure 1B). Noticeably, all the VIP cells have an IR or IR2 feature.

We consider a cell as having an Acc feature if it shows acceleration in the firing rate in all the sweeps. A looser criterion, which only requires one cell to have at least two sweeps around rheobase to show the acceleration in the firing rate, is applied to consider a cell as having an Acc2 feature. These cells with an Acc2 feature usually show acceleration when the injection current is low, but adaptation when the injection current is high (figure S1B). Cells with an Acc feature are uniquely observed in NGFCs. Further, most NGFCs are considered as having an Acc or Acc2 feature (figure 1B2), and some canopy cells are found to have an Acc2 feature (5/27).

Then, to distinguish IB and Adap, we define IB and Adap based on different time frames during the current step. We consider a cell to have an IB feature if, first, the initial firing rate is larger than $100Hz$ (first ISI is lesser than $10ms$) in all the sweeps with at least five APs; and second, the firing rate drops at least 50% in the first $100ms$ in all the sweeps. We consider a cell to have an Adap feature if the firing rate drops at least 20% from $100ms$ to $1s$ in all sweeps. The IB feature is observed in most of the $\alpha 7$ cells (20/22, the two $\alpha 7$ cells without an IB features are shown in figure 1C2), and some of the VIP cells, while Adap is observed in most of the VIP cells and some of the $\alpha 7$ cells (5/22, figure 1B3, 4). More traces of different subtypes are shown in figure S1. The

passive parameters are listed in table S1 and shown in figure S2.

In this study, we want to have parsimonious models that reproduce the spectrum of these behaviors and help understand the mechanisms behind these behaviors. To achieve these, instead of tuning our model based on the averaged features of a subtype, we decide to choose one "hero" cell from each subtype that only shows one type of the electrophysiological feature of interest and reproduce the behavior of that cell. We do this because the averaged "cell" may not be physically plausible due to the large heterogeneity within an interneuron subtype. We choose to make individual neuron models based on the exponential integrate-and-fire (EIF) neuron ([9]), but not Hodgkin-Huxley models, to minimize the number of parameters we need to tune. In the following sections, we, first, reproduce IR in a canopy cell model; second, capture the Acc and delayed spiking in an NGFC model; third, generate the IB in an $\alpha 7$ cell model. Finally, we model a VIP cell that shows IR, IB, and Adap simultaneously.

Irregular firing is reproduced in a Canopy cell model with a SIK channel

Since canopy cells with an IR feature do not have any other of the features under consideration, modeling IR on canopy cells does not need to consider the potential interactions between different features (figure 1B1). From the selected "hero" canopy cell. We observed substantial subthreshold fluctuations around $-40mV$ from the voltage traces just above the rheobase (figure 2A, B). This is more obvious in the phase diagram of the cell (figure 2C), where we plot the deviation of the voltage, which is proportional to the net current into the cell, over the voltage. A quasi-stable point is observed around $-40mV$ where the net current goes below 0, suggesting some outward current is activated during this range.

To mimic the IR at the latter $500ms$ during the current injection, we include a slow inactivating K^+ (SIK) channel in an EIF model (figure 2D, left). The major parameters of an EIF model, namely reset voltage, firing threshold, and curvature at the firing threshold can be estimated from the phase diagram directly (figure 2C), red arrows). The slow-inactivation gating variable from the SIK channel can introduce the clustered spiking, which has been known for a while ([36]). Here, the model of SIK channel follows the model of a Kv1 channel in PV+ interneurons ([28]), which contains one fast activating gating variable a and one slow inactivating gating variable b. We shift the equilibrium value of the gating variables to a more depolarized value such that the window current of this channel is around -40 mV (figure 2D, right). As argued in [28] Fig. 8, this is plausible by taking into account that the Kv1 channels are localized on the axon initial segment but not on the soma. The detailed tuning procedure is in the method section. The resulting model can reproduce the IR behavior observed in the cell (figure 2E) and the changing of IR score when the injection current varies (figure 2F). The changing of CV ISI is comparable between the data and the model (figure S4G, H). A further comparison between the data and the model is shown in figure S3 and figure S4.

Mechanism of irregular firing in the Canopy cell model

In our model, The IR feature (figure 2F) is reproduced by including a SIK channel. To understand the mechanism, we did a fast-slow analysis on our model (figure 3). Excluding the noise term by setting $\sigma = 0$, we observe clustered spiking in the model (figure 3A). We further assume the slow gating variable b is a constant and analyze the dynamics of the fast manifold defined by the voltage v and the fast activation variable a. As expected for the EIF model, the system has one stable state (SS) and one unstable steady state (US) when the injection current is low or the outward current is large

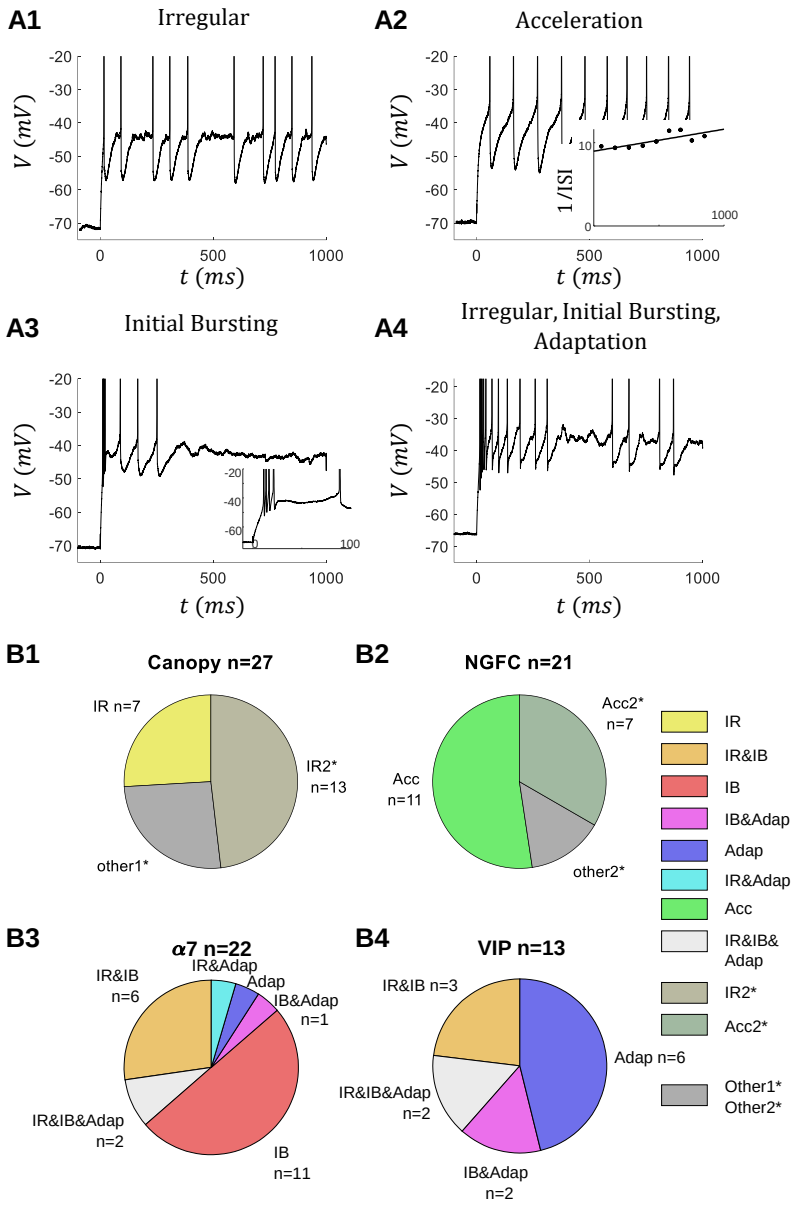

Figure 1. Dominant electrophysiological features of L1 interneuron subtypes. (A) Examples of traces that show four different types of features: irregular firing (IR), Acceleration (Acc) in the firing rate, initial bursting (IB), and adaptation (Adap) in the firing rate. In (A2), the inset shows the 1/ISI and the corresponding fitted line. In (A3), the inset shows the zoomed-in traces during the first 100ms. Traces with about 10 APs are selected as examples. (B) Distribution of the four features in different subtypes of L1 interneurons. (*) IR2 and Acc2 features are classified by looser criteria than IR and Acc, respectively (See main text). Cells with IR2 or Acc2 are only marked in the Canopy cells and NGFCs for simplicity. 11/27 Canopy cells, 4/21 NGFCs, 9/22 α7 cells, and 8/13 VIP cells have an IR2 feature. Notice all VIP cells are classified as having an IR or IR2 feature. 5/27 Canopy cells, 8/21 NGFCs, 0/22 α7 cells, and 0/13 VIP cells are classified as having an Acc2 feature. The cells that do not show any feature are indicated as "other1" or "other2". The "other2" cells are late-spiking, but "other1" cells are not. More examples are in figure S2.

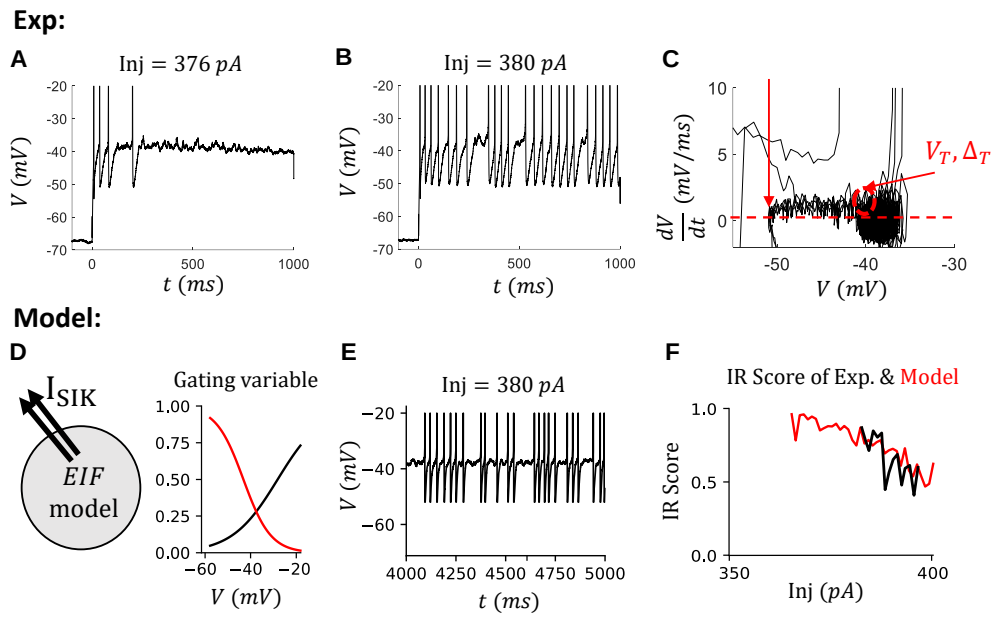

Figure 2. Modeling irregular spiking of a canopy cell with a SIK channel. (A, B) Voltage traces of an example canopy cell at Inj= $376, 380pA$, respectively. (C) Phase diagram of the cell. See fig. S3D for a zoom-out diagram. The y-axis is the slope of the voltage trace, which is proportional to the net current to the cell. Red arrows indicate where we estimate the corresponding parameters of the model. (D) The sketch of the canopy cell model (left) and the equilibrium value of the gating variables of the slow K^+ channel (right). (E) Voltage traces of the Canopy cell model at Inj= $380pA$ (F) The IR Score from the experiment (black) and the model (red).

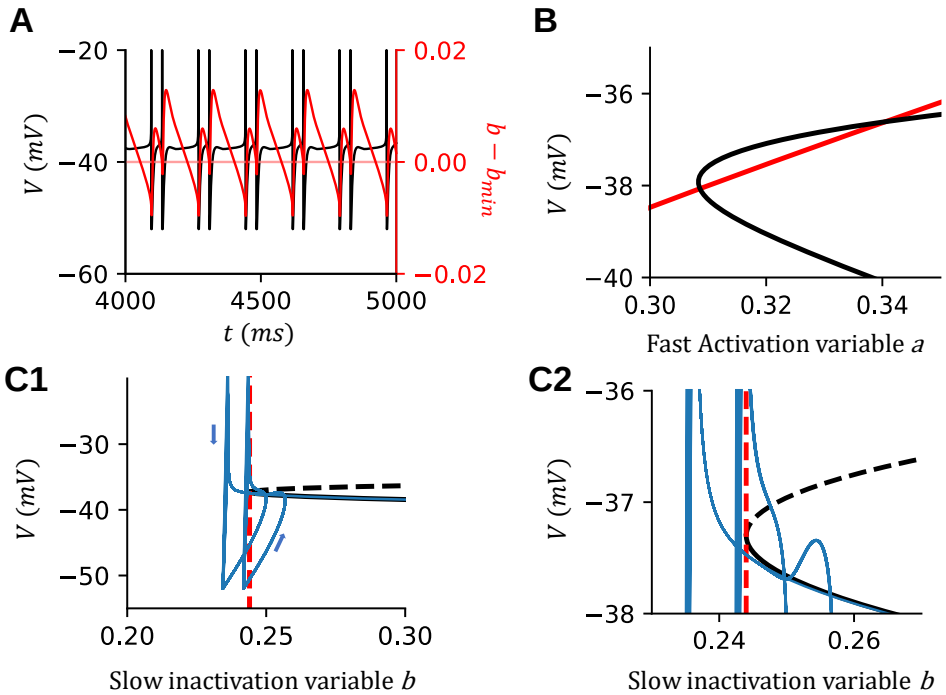

Figure 3. A fast-slow analysis of the Canopy cell model shows the irregularity is a result of the square-wave bursting. (A) Sample simulation when Inj= $375pA$ without noise. The black line indicates the voltage trace, and the red line indicates the difference between b and b_{min}. The red dashed line is at $b - b_{min} = 0$, suggesting the boundary between the resting state and the firing state of the cell. (B) Nullclines when Inj= $375pA$, $b = 0.27$. The intersections indicate the fixpoints of the fast manifold. (C) The bifurcation diagram when varying b with Inj= $375pA$. The system undergoes a saddle-node bifurcation on an invariant cycle (SNIC). The black solid and dashed lines indicate the stable branch and the unstable branch, respectively. The blue line indicates the simulation of the canopy cell model while we remove the noise term $\sigma = 0$. The red dashed line indicates the minimum b that the fast manifold has a global SS. The arrows indicate the direction of the dynamics. (C2) shows the zoomed-in dynamics around the bifurcation point.

(figure 3B). The SS branch and US branch emerge through a saddle-node bifurcation on an invariance cycle (SNIC) by increasing b over the bifurcation point b_{min}, (figure 3C). In the simulation of the full system (figure 3A, C), the slow variable b changes across the bifurcation point b_{min} over time. Thus the full system oscillates between a resting state (the global SS exists) and a spiking state (the global SS vanishes). This dynamic is known as square-wave bursting ([24], [35], [23]). Adding noise to the system $\sigma > 0$, the oscillation between the resting and spiking states mimics the IR firing patterns.

Spike frequency acceleration and delayed firing are reproduced in a NGFC model

After capturing the dynamics of IR, we next modeled the acceleration observed in an NGFC. As shown in figure 4, the Acc is accompanied by the late onset of spiking (figure 4B, C). The delay of the first spike decays when the injection current increases (figure 4D), and the firing rate slowly accelerates over the $1s$ injection period (figure 4E, F). In

the phase diagram of the cell, a similar quasi-stable point is observed around $-40mV$ (figure S5A). These dynamics suggest the presence of a slow inactivating outward current in the NGFCs.

Based on that, we tune an EIF model with the same SIK channel that has the identical dynamics as in the Canopy cell model, but with a reduced conductance to avoid the IR (figure 4G). After a similar tuning procedure, the resulting model is capable of reproducing the Acc and late-spiking observed in an NGFC (figure 4 H to L, figure S5A to F).

The delayed firing and the acceleration come from the slow inactivation gating variable b of the SIK current. To directly show that, we simulate the model with two sequential voltage steps and current steps with a variable resting time Δtime (figure S5G, H). During the first voltage step (figure S5G), the model neuron is clamped at $-40mV$. The fast-activating gating variable a opens first and increases the SIK current. Then, the slow-inactivating variable b gradually closes and decreases the SIK current. The difference between the onset and steady SIK current is about $15pA$ in our NGFC model. During a rheobase current step (figure S5H), the model neuron depolarizes to a subthreshold voltage but is held there by the fast-activating SIK current. It is only released to fire when the SIK current inactivates enough. During a current step that is above the rheobase, the SIK current also inactivates gradually, which leads to an acceleration of the firing rate. Further, the strength of the SIK current is subjected to the initial state of the slow variable b. If the second voltage step or current step is close to the first, the slow variable b does not fully restore to the open state. As a result, the peak of the SIK current and the delay of the first spike is smaller in the 2nd step compared to the 1st step (figure S5I). The initial state of b is impacted by the resting voltage, too.

Initial bursting is reproduced in an $\alpha 7$ cell model

We then studied the initial bursting behavior, which is observed in most of the $\alpha 7$ cells (figure 1B3). Cells with an IB feature show a characteristic high initial firing rate and a fast dropping of the firing rate during the first $40ms$ (figure 5A). In the phase diagram of the cell, several lines are above the spiking cycle (red arrow in figure 5B), which indicates the existence of a transient current that is less dependent on the voltage. Further, the initial firing rate is about $270Hz$ across sweeps with different injection currents. The firing rate robustly drops below $50Hz$ within $40ms$ (figure 5C).

As previously suggested ([27]) and demonstrated in ([26]), IB in $\alpha 7$ cells is depended on the expression of a T-type Ca^{2+} channel. This was also demonstrated in bursting L2/3 VIP cells ([22]). We thus include a T-type Ca^{2+} current in our EIF model for an $\alpha 7$ cell model (figure 5D) based on the reported dynamics of T-type Ca^{2+} channels from a thalamocortical relay neuron model ([30]). After tuning the conductance g_T of the T-type Ca^{2+} channel to the IB in the data, we can reproduce the high initial firing rate and the fast dropping of the firing rate during the first $40ms$ in the $\alpha 7$ cell model (figure 5E, F. See the further comparison in figure S6).

IR, IB and Adap are simultaneously reproduced in a VIP cell model

After reproducing the IR, Acc, and IB features individually, we turn to the complex dynamics observed in VIP cells. Most VIP cells show more than one considered features (figure 1B4). For example, initial bursting (figure 6A, D), irregularity (figure 6B, E), and adaptation (figure 6C, F) are observed in the same selected VIP cell. All these features can be simultaneously reproduced with an EIF model with a T-type Ca^{2+} channel, a SIK channel, and a spike-triggered small conductance K^+ channel (figure 6G).

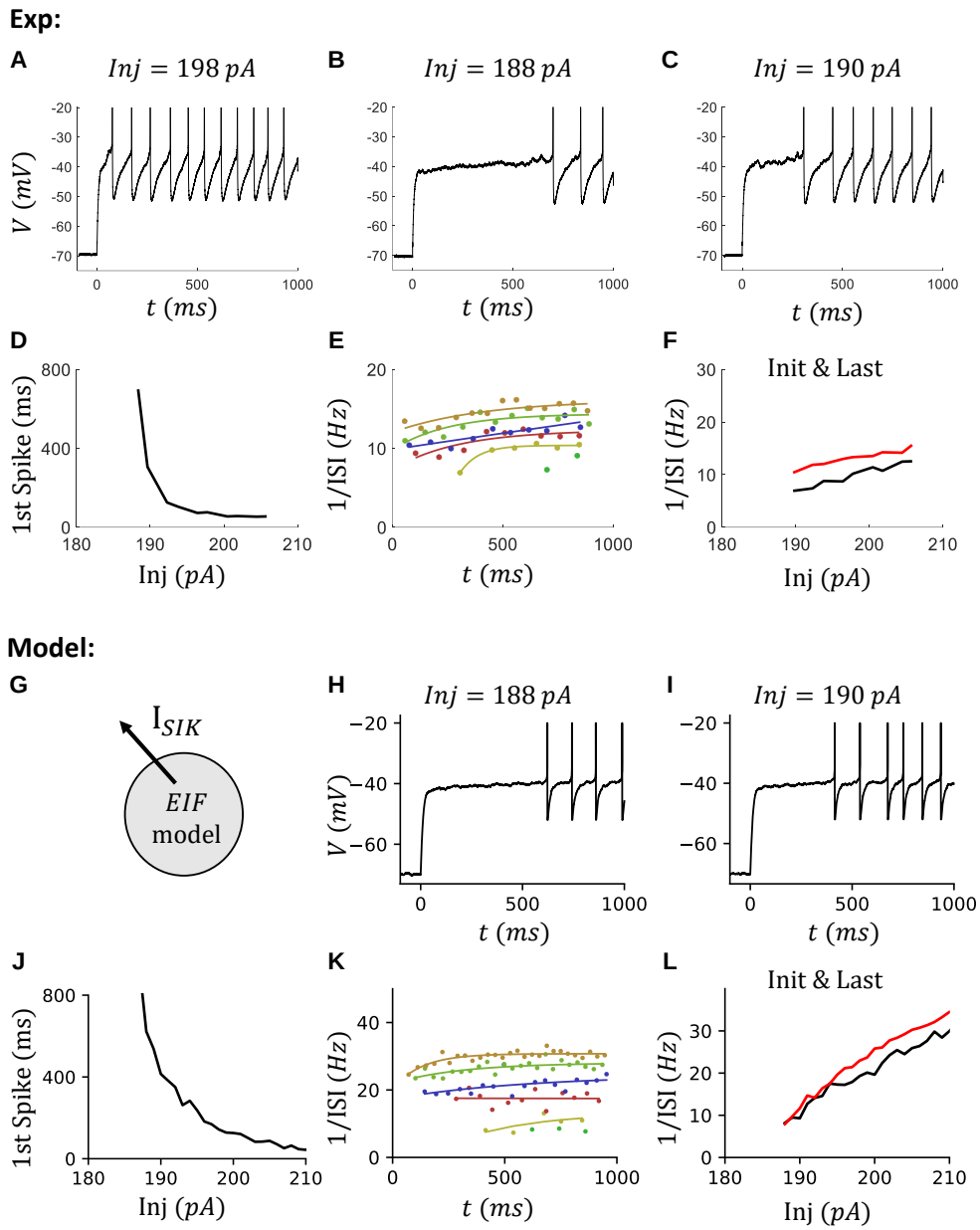

Figure 4. Modeling the acceleration and late-spiking of an NGFC with a smaller SIK conductance. (A to C) Voltage traces of the selected NGFC at Inj= $198, 188, 190pA$. (D) The time of the first spike decreases when increasing the injection current. (E) The instantaneous firing rate as 1/ISI over time. We fit the ISIs (dot) to an exponential decay curve (line) for different injection currents Inj= $188, 190, 194, 198, 202, 206pA$ (color). (F) The initial firing rate (black) and the last (red) firing rate at different injection currents. (G) The sketch of the NGFC model. (H to L) are organized as (B to F).

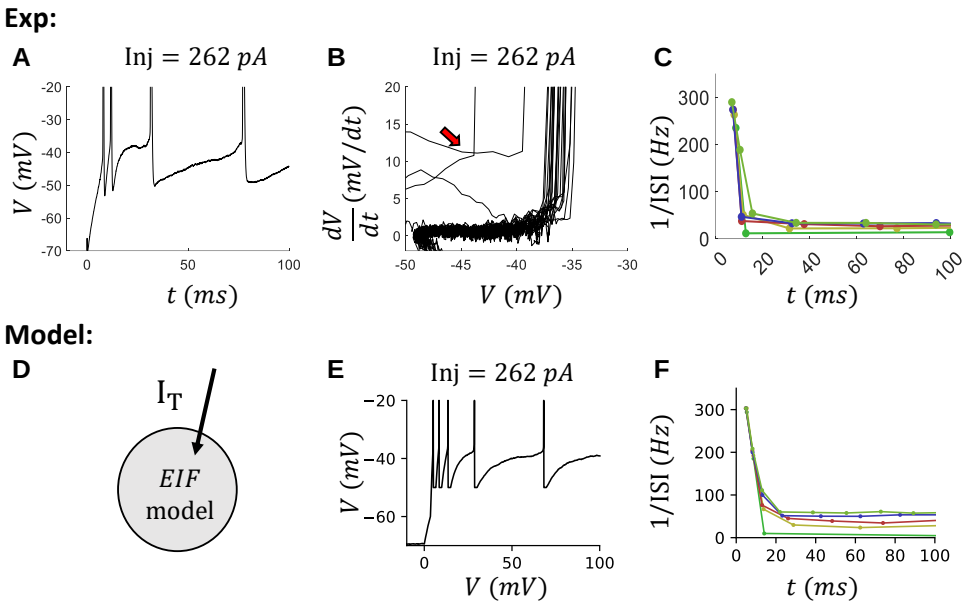

Figure 5. Modeling the initial bursting of an $\alpha 7$ cell with a T-type calcium channel. (A) The voltage trace at Inj= $192pA$. (B) Phase diagram of the cell. (C) Instantaneous firing rate shows a sudden drop in the first $40ms$ of the injection period. Colors suggest sweeps with different injection currents Inj= $252, 262, 272, 282, 292pA$. (D) The sketch of the $\alpha 7$ cell model (E, F) Modeling results organized as (A, C).

As described in the modeling of an $\alpha 7$ cell (figure 5), the IB has the characteristic high initial firing rate and a fast dropping in the firing rate during the first $40ms$, and transient lines in the phase diagrams (figure S7 A, B). This was reproduced by tuning the conductance g_T of the T-type Ca^{2+} channel in the $\alpha 7$ model.

In addition, the IR score is highest in the sweeps around rheobase, and it decays slowly with increasing current injection (figure 6E). The IR score remains higher than 0.4, which is the threshold to detect IR, even in a $1s$ sweep with 60 APs with injection current Inj= $300pA$ (figure S7F). Above, we reproduced IR spiking by including a strong SIK current in the Canopy cell model. However, the IR score drops fast in the Canopy cell model when increasing the injected current (figure 2F, figure S4H).

Strong adaptation is also observed in the VIP cell in the last $900ms$ (figure 6C), where the firing rate drops exponentially to a saturation value (figure 6F). To quantify that, we define the adaptation index (AI) as the fraction of the firing rate that drops during this $900ms$ period. For this VIP cell, AI is about 0.5 in all the sweeps (figure S7G). To reproduce the adaptation, we include a spike-triggered small conductance K^+ channel in our model (figure 6G) that generates after-hyperpolarization (AHP) current reproducing current-independent adaptation in pyramidal cells ([18]).

After a similar tuning of the VIP cell model, we can reproduce simultaneously the IB, which is reflected in the high initial and the fast-dropping of the firing rate during the first $40ms$ (figure 6J), IR, which is reflected by the high IR score and high CV of the ISIs (figure 6K), and Adap, which shows exponentially decay during the latter $900ms$ (figure 6L, figure S7G).

However, there are limitations to this VIP cell model. First, though the irregularity during the steady-state is similar between the data and the model, the onset of irregular firing in the model is usually later than that in the data. Especially when the injection

current is around the rheobase, the irregular firing may be observed after $1s$ in the model (figure S8A). In contrast, in the data, it may be observed between $500ms$ to $1s$ (compare figure 6B). Second, the cell in the model becomes quiescence after the IB period (around $100ms$), which results from the strong adaptation current triggered by several APs during the initial bursting and the fast activation of the SIK current. But this is not the case in the data (figure 6B). In the model, this quiescence period diminishes when the injection current is high enough inj= $235pA$ (figure S8C). Since we are measuring the adaptation starting at $100ms$, the diminishing of the quiescence period is reflected in the initial firing rate after $100ms$ (figure S8D) and is further reflected in the jump of the adaptation current (figure S7G).

To get an insight into what impacts firing after the IB period, we change the timescale of the fast activation variable of the SIK channel, which delays the onset of outward SIK current (figure S8E). As expected, the firing after the IB continues. But to achieve a comparable length with the data, the timescale needs to be around $80ms$, which is unlikely for a SIK channel. We discuss the discrepancy further in the discussion section.

Mechanism of irregular firing in the VIP cell model

To investigate the origin of IR in the VIP cell model, we do a similar fast-slow analysis as we did for the canopy cell model. We first exclude the noise term in the model by setting $\sigma = 0$ and observe cluster spiking in the simulation (figure 7A). In contrast to the canopy cell model, we have two slow variables: slow inactivation variable b and the dimensionless Ca^{2+} concentration C_{ca}. To do the fast-slow analysis, we assume both are constants. Similarly, the system has one SS and one US when either outward current prevails the injection current (figure 7B). By assuming C_{ca} a constant, we can define the $b_{min}(C_{ca})$ as the minimal b where a global SS exists (figure 7C, red dashed lines). In the full system, the line $b_{min}(C_{ca})$ represents the line where the SNIC bifurcation happens (figure 7D, red dashed lines). Only in the region above the bifurcation line, a global SS exists. In the simulation of the full model (figure 7A, D), the system oscillates between a resting state and a spiking state, which is represented as cluster spiking. The dynamics change to irregular firing when adding noise to the system by setting $\sigma > 0$.

Mechanism behind the traditional alias "irregular spiking cell" for VIP cells.

Traditionally, the term irregular spiking has been used mainly for VIP cells but rarely for other INs ([34]). But, in our study, we find irregularity is not uniquely found in VIP cells but distributed in multiple subtypes of L1 interneurons. Especially, the IR in the VIP cells is not due to a higher noise level. In fact, the noise levels around the rheobase are comparable across all the subtypes (figure S3G, S5C, S6C, S7E). Is there anything unique for the IR VIP cells but not other INs with an IR feature?

To answer this question, we systematically vary the parameters of our VIP cell model. We measure the IR score while varying adaptation strength γ and conductance of the SIK channel at different injection currents (figure 8A, B). The IR score is higher when the SIK conductance is bigger. Interestingly, the high IR score is more spread out with a stronger adaptation. To quantify this effect, we define IR width as the range of injection current where the IR score is bigger than the threshold 0.6 (figure 8C). As a result, we observed that the IR width only starts increasing when g_{SIK} reaches around $100nS$ (figure 8D). Further, on the one hand, without adaptation current, the IR width is low no matter the value of g_{SIK}. On the other hand, increasing the adaptation strength can dramatically increase the range of IR width. The trend is similar if we use the IR area-under-the-curve (AUC) instead of IR width (figure S9C). Further, without

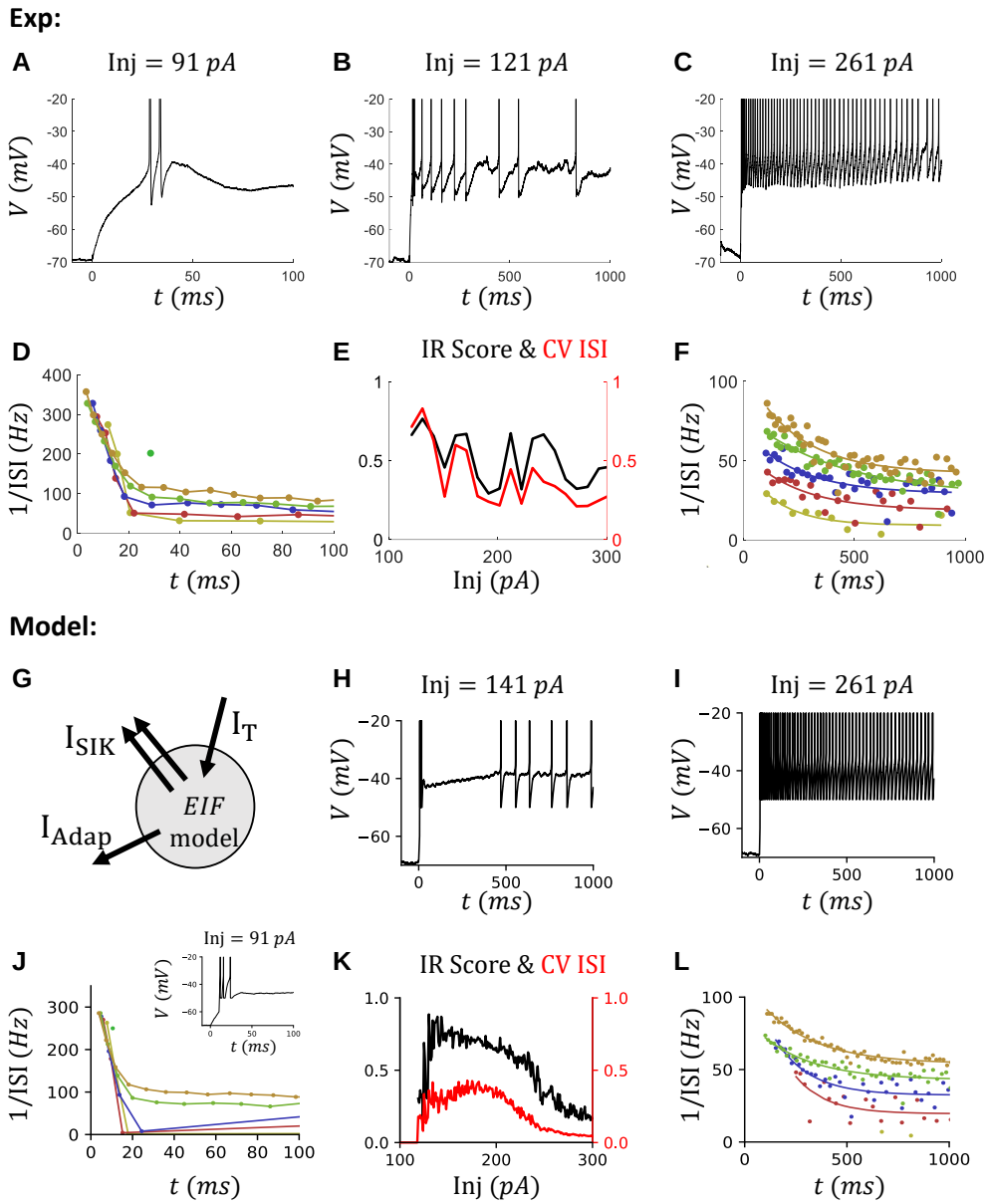

Figure 6. Reproducing the initial bursting, irregular firing patterns, and adaption simultaneously in a VIP cell model. (A to C) Voltage traces at Inj= $91, 121, 261pA$, which are examples to show IB, IR, and Adap, respectively. (D) The instantaneous firing rates during $0ms$ to $100ms$ show the initial bursting. Colors represent sweeps with different injection currents Inj= $91, 131, 171, 212, 251, 291pA$. (E) The ISI ratio (black) and CV ISI (red) curves, which show the irregularity. (F) The instantaneous firing rates between $100ms$ to $1s$, which show the adaptation. Color coding is the same as (D). (G) Sketch of the VIP cell model. (H to L) Modeling results organized as (B to F). The inset of (J) shows the voltage trace at $91pA$ between $-10ms$ to $100ms$ from the model.

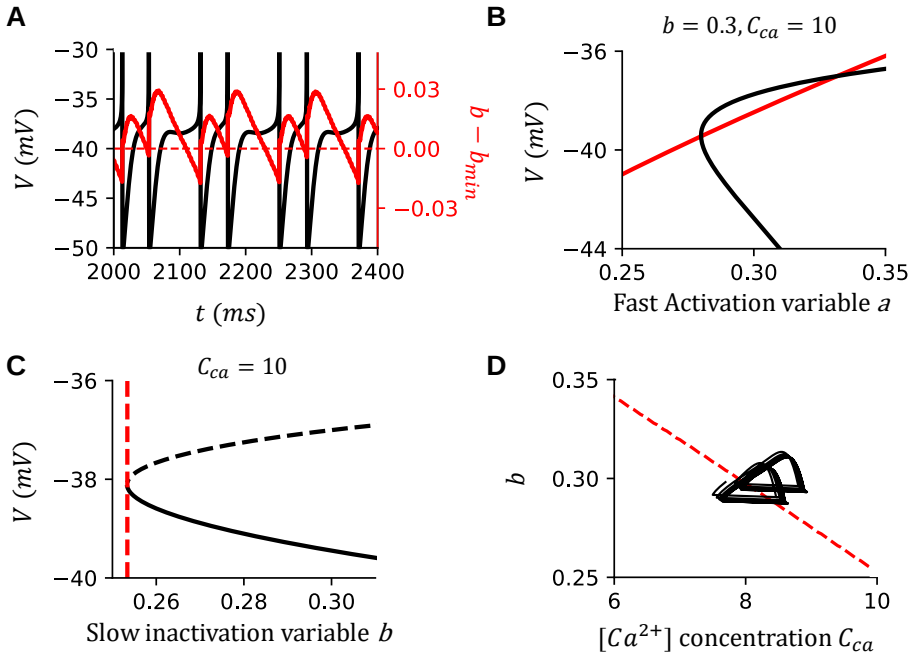

Figure 7. The fast-slow analysis of the VIP cell model shows the irregularity is a result of the square-wave bursting. (A) The sample simulation when Inj= $170pA$. The black line indicates the voltage trace, and the red line indicates the difference between b and b_{min}. The red dashed line is at $b - b_{min} = 0$, suggesting the boundary between the resting state and the firing state. (B) Nullclines of the fast manifold when Inj= $170pA$, $C_{ca} = 10$, $b = 0.3$. The intersections indicate the fixpoints of the fast manifold. (C) The bifurcation diagram when Inj= $170pA$, $C_{ca} = 10$. The black solid and dashed lines indicate the stable branch and the unstable branch, respectively. The red dashed line indicates the minimum of b that the fast manifold has a global SS. (D) The bifurcation diagram of the whole system and the simulation when Inj= $170pA$. The red dashed line $b_{min}(C_{ca})$ indicates the SNIC bifurcation line. Only the region above which has a global SS. The black line indicates the simulation of the VIP cell model without noise ($\sigma = 0$).

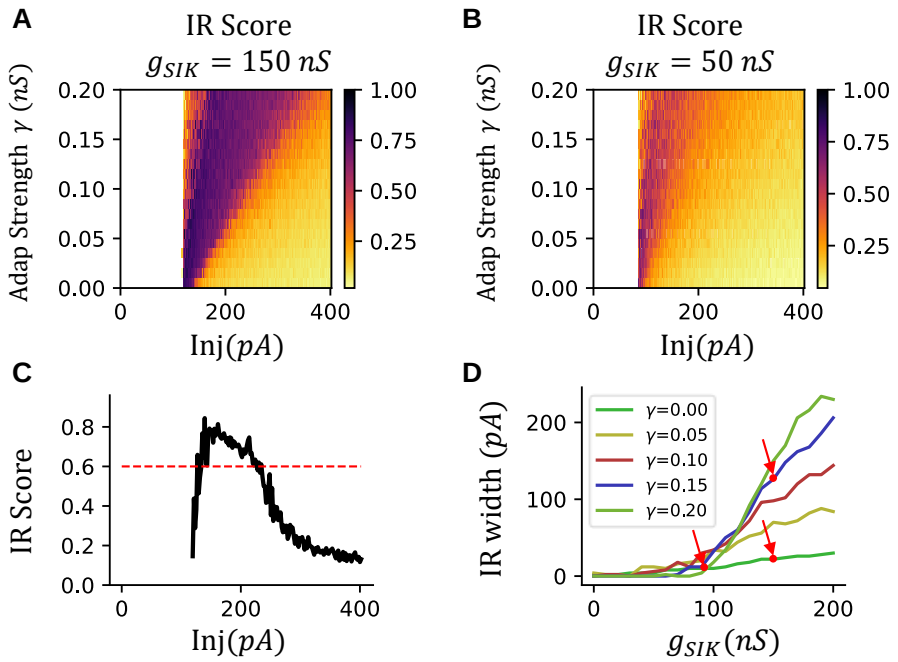

Figure 8. The irregular firing of VIP cells is more easily observed in experiments because of a large irregular width introduced by the interaction between I_{SIK} and I_{adap}. (A) The ISI ratio (color) over different injection current I_{adap} and adaptation strength γ when $g_{SIK} = 150nS$. (B) as (A) but $g_{SIK} = 50nS$. (C) The sample ISI ratio when $g_{SIK} = 150nS, \gamma = 0.1$. The range of injection current when CV ISI is above the threshold 0.6 is defined as the irregular width (IR width). (D) The IR width curves over g_{SIK}. Different lines suggest results with different adaptation strength γ.

adaptation current, the IR width is low with any g_{SIK}, while increasing the adaptation strength can dramatically increase the range of IR width. In the VIP cell model, the IR width is around $120pA$ (right top arrow in figure 8D). By removing the adaptation current, the IR width decreases drastically to around $20pA$ (right bottom arrow in figure 8D), where the dynamics mimic the IR in Canopy cells (figure S9A). If in addition we decrease g_{SIK}, the IR width decreases to about $10pA$ (left arrow in figure 8D), where the dynamics mimic the Acc in NGFC (figure S9B). These results suggest that IR is most easily observed only when the g_{SIK} is big and the adaptation is strong, which is the case for VIP cells but not other INs.

To verify this claim in our dataset, we measured the IR width by multiplying the number of sweeps with IR score bigger than 0.4 by the corresponding current step size of IR cells in different IN subtypes. The average IR width for VIP cells is the highest, and it is much higher than that for canopy cells (table S1). Furthermore, the input resistance is the highest of the VIP cells compared to other L1 INs (table S1), including $\alpha7$ cells. Even though the IR width of VIP cells and $\alpha7$ cells are comparable, the corresponding voltage change of VIP cells is much higher than that of $\alpha7$ cells, which explains why the IR feature is most salient in VIP cells.

Discussion

The neocortex is characterized by a remarkable diversity of GABAergic interneuron subtypes ([21]). Their functions have been proposed to serve diverse functions, exemplified by the well-established disinhibitory motif composed of three inhibitory subtypes ([37], [34]). In this study, we systematically analyze the distribution of electrophysiological features in the L1 IN subtypes and further build models for each subtype by including different ion channels. Canopy cells and NGFCs mostly show irregular firing or acceleration in the firing rate, suggesting the existence of SIK in these two cell types. most of the $\alpha 7$ cells are classified as having an initial bursting feature, which implies the presence of a T-type Ca^{2+} channel. The VIP cells are very heterogeneous, but many of the cells show adaptation and irregular firing. To reproduce that, we build a model that includes a SIK channel, a T-type Ca^{2+} channel, and a spike-triggered Ca^{2+}-dependent K^+ channel. We apply slow-fast analyses to show that the irregularity comes from the square-wave bursting, which requires a strong SIK current. Further, we showed that the adaptation current observed within the VIP cells significantly expands the region where the irregular firing can be observed, and that is the main reason why VIP cells are often considered "irregular spiking cells", but not other INs ([34]).

Our work provides insights into outstanding questions concerning interneuron subtype biology. First, by revealing the mechanism of IR firing of VIP cells, applying an antagonist to either block the SIK channel or the adaptation current should eliminate the irregular firing. Applying gene-editing methodology in cultured cells should show similar results as well. Second, our VIP model suggests that the different electrophysiology subtypes from VIP cells may come from continually varying the strength of different ion currents, thus contributing to the classification of VIP subtypes. For instance, the cells classified as IS, fAD, and bNA in ([15]) may be reproduced by just including a strong SIK current, a strong T-type Ca^{2+} channel with or without a strong adaptation current, and a combination of T-type Ca^{2+} current with a SIK current, respectively.

Late-spiking is a signature of neurogliaform cells, but the underlying mechanism is unknown. In delayed-firing hippocampal CA1 pyramidal neurons ([32]), blocking a SIK current with low concentrations of 4-aminopyridine (4-AP), which blocks Kv1 currents, eliminates the delayed-firing feature. Further, in delayed fast-spiking cells, a dendrotoxin sensitive Kv1 current underlies the delayed firing ([13], see also [2]) and clustered spiking with subthreshold oscillations ([28]). Based on these experiments, we adapted the dynamics of Kv1 channels in our NGFC model and we were able to reproduce the late-spiking and the acceleration in the firing rate. However, a recent study on NGFCs suggested that even though Kv1 currents exist in the mouse NGFCs and contribute to the delayed-firing ([5] fig. 4I, applying low 4-AP decreases about 65% of the AP latency), their functional role may be lesser than that of other K^+ currents, especially from the Kv4 family. Furthermore, preliminary results from our lab suggest that dendrotoxin does not block delayed firing in NGFCs. Interestingly, the recovery time from inactivation is about $1s$ in [5] and about $12s$ in [2], which is faster than that in our model (about 500 ms, fig. S5I). Nevertheless, this discrepancy is not likely explained by the dynamics of Kv4 channels, which is faster than that of Kv1 channels ([6]). Further pharmacological experiments are necessary to help discover the slowly inactivating K^+ current of NGFCs.

We choose to build our models based on an EIF model with a few additional ion channels to reproduce the major observed dynamics. Thus, the models are easy to analyze, and the computational cost is minimized when implemented in a large-scale neuronal circuit. However, doing so limits the capability to reproduce every experimental electrophysiological feature. Unlike Hodgkin-Huxley type models, our

model doesn't include the dynamics during the APs. Thus we cannot connect the features of APs from different subtypes (see table S1) to the expression level of Na^+ channels and K^+ channels in our model. Another major issue is that we mostly reproduce the firing behavior around the rheobase but not the region where the firing rate is large ($> 20Hz$). This is a limitation of our database and the innate property of the EIF type model. On the one hand, within our dataset, only a small fraction of cells have sweeps with more than 30 APs, and only a handful of cells reach the maximum firing frequency. Further, again, the heterogeneity is considerable even among the same L1 subtype when the depolarization current is strong (supp figure S2). As a result, we cannot draw meaningful statistics to describe the behavior in this range. On the other hand, unlike the Hodgkin-Huxley type model where the firing stops when the injection current overwhelms the outward $K+$ currents, the firing rate can go arbitrarily high in the EIF model. As a result, the capability to reproduce the behavior is limited around the maximum firing rate, which is relatively low in the L1 INs. In addition, readers should be aware that the f-I slope in our model is higher than that measured from data. From our experience, the only parameter in our model that significantly impacts the f-I slope is the capacity, which is constrained by the data (supp figure S2, table S1). We suspect this mismatch comes from the simplicity of our model, because multiple outward currents may exist in reality and decrease the slope of the firing rate, like K^+ current from KCNQ channels ([12]).

A significant difference between NGFCs and Canopy cells is that NGFCs are late-spiking whereas Canopy cells are not. However, if Canopy cell models only include a SIK channel, then they are late-spiking as well (figure S4). This discrepancy remains to be understood as well as the difference in firing following the IB period in VIP cells and in our model. VIP cells often show decreased firing rates after the IB period, usually around $100ms$, but are not quiescent (figure 6B). This behavior was also hard to reproduce in the model, due to the large adaptation current introduced by several APs in the IB period. These discrepancies in the Canopy model and the VIP model suggest the existence of transient inward currents (or inactivation of outward currents) that have slower dynamics than the T-type Ca^{2+} current. In VIP cells ([12]), the Nav1.1 channel may contribute to the length of the initial firing period via progressive inactivation during repetitive firing. To validate the role of Nav1.1 channels in models with an IR feature, further experiments and modeling studies are required.

Recently, it has become clear that L1 is the key to understanding how long range cortical-cortical interactions alter local circuit dynamics ([26], [17]). For example, recent work in rodents showed that hippocampal-dependent associative learning is controlled by perirhinal input to L1 ([7], [29]). More importantly, this associative learning can be diverted by dendritic inhibition. Another recent study had shown that L1 NDNF+ INs (NGFCs and Canopy cells in our study) can shift the input gain from dendrite to soma in pyramidal cells across all layers in the cortex ([20]), suggesting L1 NDNF+ INs may be well-suited to control associative learning. Further, another anatomical study showed that ventromedial and mediodorsal thalamus target NDNF+ cells and VIP+ cells in mouse prefrontal cortex, respectively ([1]), through which these higher-order thalamic nuclei differentially modulate the neuronal activity in the prefrontal cortex. To further investigate the hypotheses listed here and beyond, a well-developed model that incorporates the distinct properties of each L1 interneuron subtype will help in elucidating the mechanisms by which the L1 circuit enables the integration of top-down and bottom-up information streams, and will assist in the generation of predictions to guide future experiments. Our work on the individual L1 IN subtypes here is an essential step towards this goal.

Methods and Materials

The L1 interneuron data used in this study were collected previously in [27]. To measure the firing patterns, the cells were first held at about $-70mV$, then injected with square-wave depolarization current for 1s. The original pClamp data is analyzed in Matlab by using a self-developed package. The cells of which the maximum spike count in all the sweeps is less than ten during the 1s current step are excluded in this study.

AP detection and ISI

The spikes are detected when the voltage trace $V(t)$ crosses a detection threshold V_{det}. This threshold is determined as follows: We first set up a upper bound as $V_{up} = \min\{\max(V(t)), 0mV\}$, then a lower bond as V_{low} =median$(V(t))$. Next, we set the detection threshold as $V_{det} = \max\{0.8V_{up} + 0.2V_{low}, -20mV\}$. The ending detection threshold V_{det} is within the range $-20mV$ to $0mV$, and it is robust when the AP maximum voltage and AP threshold vary across different cells. The ith AP is detected at t_i if $V(t_i) < V_{thr}$ and $V(t_i + \Delta t) \geq V_{thr}$, with the resolution in our recordings $\Delta t = 0.05ms$. We further exclude any noise-introduced detections within $0.5ms$ following another AP.

We calculate the ISI as $\text{ISI}(t_i) = t_{i+1} - t_i$. We define instantaneous firing (IF) rate as 1/ISI. In some cases, we fit the curves of instantaneous firing rate to an exponential function $a + b\exp(-cx)$ by using the Matlab build-in function fit.

Criteria for electrophysiological features

IR: The IR score and CV ISI are calculated for the sweeps with more than 5 spikes during $500ms$ to $1s$. The IR score of a pair of ISIs is defined as $1 - \min\{\text{ISI}(t_i)/\text{ISI}(t_{i+1}), \text{ISI}(t_{i+1})/\text{ISI}(t_i)\}$, where $t_i > 500ms$. To exclude the potential impact from noise, only the cells with three different ISI pairs, in all the sweeps of the cell, of which the IR score is bigger than the threshold 0.4, are classified as having an IR feature. The IR score of a sweep is defined as the maximum IR score of all ISI pairs of the sweep. CV ISI=$std(\text{ISI}(t_i))/mean(\text{ISI}(t_i))$, where $t_i > 500ms$. If a cell only has one ISI pair, of which IR score is bigger than the threshold during $200ms$ to $1s$, but is not classified as having an IR feature, the cell is classified as having an IR2 feature. In the model, the IR score and CV ISI are measured from $3s$ to $5s$ during the injection period. The IR width is only measured for the cells with an IR feature. It is defined as the number of sweeps with an IR score bigger than the threshold 0.4 times the current step ΔI_{inj} of the corresponding recordings.

Acc: We do a linear regression on the curve of 1/ISI for each sweep to calculate the slope. A cell is classified as having an Acc feature if its slopes from all the sweeps are positive. If a cell has more than two positive slopes (at least two sweeps are accelerating) but is not classified as having an Acc feature, the cell is classified as having an Acc2 feature.

IB: We fit the corresponding IF curve to an exponential decay function for the sweeps from a given cell with at least four spikes (three ISIs) during the first $100ms$ of the current injection. If all the fitted IF curves drop at least 50% during this $100ms$, and if the first ISI in all these sweeps is lesser than $10ms$, which suggests the initial IF is bigger than $100Hz$ for all these sweeps, the cell is classified as having an IB feature.

Adap: we fit the IF curves of a given cell during $100ms$ to $1s$ to an exponential function $f_{adap}(t)$ for the sweeps with more than six spikes (five ISIs) during this period. The fraction of the dropped firing rate is defined as Adaptation Index (AI= $1 - f_{adap}(1s)/f_{adap}(100ms)$). If the fitted IF curve drops at least 20% (AI> 0.2) in $900ms$ for all the sweeps, the cell is classified as having an Adap feature.

Measurements of electrophysiological properties

The time constant τ of a cell is calculated by fitting the voltage trace from the $100ms$ following the end of the sag step to an exponential decay function on each sweep, then averaging across all the sweeps. Resistance R is calculated by first dividing the voltage difference (ΔV) over the current differences (ΔI_{inj}) before and during the sag step, then averaging across all the sweeps. Capacity C is calculated by dividing the timescale over the resistance in each sweep and then averaging across all the sweeps.

The delay of the first spike is defined as the time of the first spike of the sweep to current injection onset, measured at the sweep with the lowest injection current and at least 2 APs, such that we exclude the possibility that a single spike is triggered by large fluctuation just below the rheobase. We analyze the slope and rheobase of the firing rate curve (f-I curve) by fitting the spike counts during $1s$ to a ReLU function $f(I) = k \max\{I - I_0, 0\}$, where the resulting k is reported as the f-I slope and I_0 as the rheobase. Only the sweeps with lesser than $40Hz$, or the first sweeps with APs are used to do the ReLU fitting, such that the fitted curve better represents the behavior around the rheobase.

To measure the properties of APs, we exclude the first two APs, which limits the effect of APs during the initial bursting, and combined remained APs from all the sweeps of which spike count is less than 40. For each AP, the maximum voltage is calculated from the $2ms$ time window following the trace past the AP detection threshold; then, all the APs are aligned by setting $t = 0$ when the voltage reaches the maximum. Maximum rise and decay slopes are calculated during $[-1ms, 10ms]$. The AP reset is calculated as the minimum voltage during $[0, 10ms]$. The AP threshold is calculated as the voltage when the voltage deviation is $20mV/ms$. The halfwidth of AP is calculated as the time of the AP above the midpoint between the maximum voltage and the threshold. Linear interpolation is used in calculating the threshold and halfwidth to improve resolution. Then, all these properties are averaged across all the APs from a cell.

All the measured properties are listed in table S1. Some values are not identical as in [27] because we exclude cells with fewer than ten spikes.

EIF models

We implement our models in Python3.9 with the Brian2 package. We use the default ODE solver in Brain2 with the a timestep $dt = 0.1ms$. Following [9], our EIF models have the form

$$C\frac{dV}{dt} = -((V - V_L) + \Delta_T \exp(\frac{V - V_T}{\Delta_T}))/R + < \text{other currents} > +\sigma, \tag{1}$$

where V represents the voltage; C, R are the passive parameters, capacity, and input resistance; V_L is the reversal potential; V_T is the voltage threshold, and Δ_T is the curvature at V_T; σ is a Gaussian noise term. Notice the voltage threshold is not the same as the AP threshold measured from the data. All the models have a $2ms$ refractory period after each AP. In addition, we have included different currents to reproduce the rich dynamics of L1 interneurons.

To reproduce the IR and Acc, we include a SIK current as in [28] dynamics:

$$I_{SIK} = -g_{SIK} a^3 b (V - V_k), \tag{2}$$

$$\tau_a \frac{da}{dt} = a_{inf} - a = \frac{1}{1+exp(-(V-a_{mid})/a_{sig})} - a, \tag{3}$$

$$\tau_b \frac{db}{dt} = b_{inf} - b = \frac{1}{1+exp(-(V-b_{mid})/b_{sig})} - b. \tag{4}$$

where $V_k = -90mV$, $\tau_a = 6ms$, $\tau_b = 150ms$, $a_{sig} = 10mV$, $b_{sig} = -6mV$, $a_{mid} = -50mV + V_\mu$, $b_{sig} = -65mV + V_\mu$. We shifted the mid point of equilibrium curve a_{inf}, b_{inf} by $V_\mu = 20mV$ to have the desired window currents. We vary the conductance g_{SIK} in different models.

To reproduce IB, we include a T-type Ca^{2+} current as in [30]:

$$I_T = -g_T m_{T,\infty} h_T (V - V_{ca}), \tag{5}$$

$$m_{T,\infty} = \begin{cases} 1 & , V > V_h, \\ 0 & , V < V_h, \end{cases} \tag{6}$$

$$\frac{dh}{dt} = \begin{cases} -h/\tau_h^- & , V > V_h, \\ (1-h)/\tau_h^+ & , V < V_h, \end{cases} \tag{7}$$

$$\tag{8}$$

where $V_{ca} = 120mV$, $V_h = 60mV$,$\tau_h^- = 5ms$, $\tau_h^+ = 100ms$.

To reproduce Adap, we include a spike-triggered Ca^{2+} dependent K^+ current, as in [18]:

$$I_{Adap} = -\gamma C_{ca}(V - V_k), \tag{9}$$

$$\tau_{ca}\frac{dC_{ca}}{dt} = \textstyle\sum_i \delta(t - t_{spike}^{(i)}) - C_{ca}, \tag{10}$$

$$\tag{11}$$

where C_{ca} represents a dimensionless Ca^{2+} concentration in the cell. It jumps by 1 after each spike at $t_{spike}^{(i)}$. $\tau_{ca} = 500ms$.

Tuning procedure

We first adopt the passive parameters, namely capacity C and input resistance R, measured from the data. We take the resting voltage as the clamping voltage in the data, which is about $-70mV$. Then, we estimate the reset voltage, threshold, and curvature from the phase diagram of the cell, like figure 2C. Further, we estimate the noise term σ based on the standard deviation of voltage before or just above the rheobase current during $500ms$ to $1s$ of the depolarization current step (figure S3G, figure S4D). In addition, we consider the change of the gating variable during the APs. We can estimate the change of the slow variable Δb after each AP by solving the differential equation of b while replacing the voltage term by the shape of AP (figure S3H, I). The initial value of b is chosen based on our simulation. This is plausible because the dynamics of b are much slower (time constant $\tau_b = 150ms$) than the time window of APs (refractory period of the model $2ms$). Choosing different Δb in the model has little impact on the simulation results. Since the jump of the fast variable Δa doesn't change the dynamics of the model due to the rapid convergence to the equilibrium point ($\tau_a = 6ms$), we set $\Delta a \equiv 0$.

Importantly, we tune the conductance g_{SIK} of the SIK channel based on the IR score curve, acceleration, and delay of the 1st spike; we modify the conductance g_T of T-type Ca^{2+} based on the firing rate during IB, and we choose the strength of adaptation γ based on the AI curve.

We further adjust all the parameters in the model to best reproduce other cell features, namely the rheobase, the slope of the f-I curve, and the firing behavior of individual sweeps.

All parameter values of the model are listed in table 1 and shown in figure S10.

	Canopy	NGFC	$\alpha 7$	VIP
Resistance R (MΩ)	86	163	120	400
Capacity C(pF)	80	80	80	80
Reversal potential V_L (pF)	-67	-70	-70	-69
Threshold V_T (pF)	-38	-40	-39	-40
Reset voltage V_T (pF)	-52	-52	-50	-50
Curvature Δ_T (mV)	1	1	0.5	1
Noise Std σ (pA)	20	8	10	10
Conductance g_{SIK} (nS)	120	30	/	150
Jump of slow gating variable Δb	-0.002	-0.004	/	-0.001
Conductance g_T (nS)	/	/	8	10
Adaptation Strength γ (nS)	/	/	/	0.1
Rheobase (pA)	366.2	177.5	244.3	177.7
f-I slope (Hz/pA)	1.64	0.933	1.28	0.33

Table 1. Parameters used in the models. The rheobase and f-I slope are measured by fitting the curve of firing-rate at the steady state to a ReLU function.

References

1. P. G. Anastasiades, D. P. Collins, and A. G. Carter. Mediodorsal and ventromedial thalamus engage distinct l1 circuits in the prefrontal cortex. *Neuron*, 109(2):314–330, 2021.

2. R. Bos, R. M. Harris-Warrick, C. Brocard, L. E. Demianenko, M. Manuel, D. Zytnicki, S. M. Korogod, and F. Brocard. Kv1. 2 channels promote nonlinear spiking motoneurons for powering up locomotion. *Cell reports*, 22(12):3315–3327, 2018.

3. B. Cauli, E. Audinat, B. Lambolez, M. C. Angulo, N. Ropert, K. Tsuzuki, S. Hestrin, and J. Rossier. Molecular and physiological diversity of cortical nonpyramidal cells. *Journal of Neuroscience*, 17(10):3894–3906, 1997.

4. L. Cauller. Layer i of primary sensory neocortex: where top-down converges upon bottom-up. *Behavioural brain research*, 71(1-2):163–170, 1995.

5. R. Chittajallu, K. Auville, V. Mahadevan, M. Lai, S. Hunt, D. Calvigioni, K. A. Pelkey, K. A. Zaghloul, and C. J. McBain. Activity-dependent tuning of intrinsic excitability in mouse and human neurogliaform cells. *Elife*, 9:e57571, 2020.

6. W. A. Coetzee, Y. Amarillo, J. Chiu, A. Chow, D. Lau, T. McCormack, H. Morena, M. S. Nadal, A. Ozaita, D. Pountney, et al. Molecular diversity of k+ channels. *Annals of the New York Academy of Sciences*, 868(1):233–255, 1999.

7. G. Doron, J. N. Shin, N. Takahashi, M. Drüke, C. Bocklisch, S. Skenderi, L. de Mont, M. Toumazou, J. Ledderose, M. Brecht, et al. Perirhinal input to neocortical layer 1 controls learning. *Science*, 370(6523):eaaz3136, 2020.

8. R. D. D'Souza and A. Burkhalter. A laminar organization for selective cortico-cortical communication. *Frontiers in neuroanatomy*, 11:71, 2017.

9. N. Fourcaud-Trocmé, D. Hansel, C. Van Vreeswijk, and N. Brunel. How spike generation mechanisms determine the neuronal response to fluctuating inputs. *Journal of neuroscience*, 23(37):11628–11640, 2003.

10. M. Galarreta, F. Erdélyi, G. Szabó, and S. Hestrin. Electrical coupling among irregular-spiking gabaergic interneurons expressing cannabinoid receptors. *Journal of Neuroscience*, 24(44):9770–9778, 2004.

11. M. Garcia-Munoz and G. W. Arbuthnott. Basal ganglia—thalamus and the "crowning enigma". *Frontiers in neural circuits*, 9:71, 2015.

12. K. M. Goff and E. M. Goldberg. Vasoactive intestinal peptide-expressing interneurons are impaired in a mouse model of dravet syndrome. *Elife*, 8:e46846, 2019.

13. E. M. Goldberg, B. D. Clark, E. Zagha, M. Nahmani, A. Erisir, and B. Rudy. K+ channels at the axon initial segment dampen near-threshold excitability of neocortical fast-spiking gabaergic interneurons. *Neuron*, 58(3):387–400, 2008.

14. N. W. Gouwens, S. A. Sorensen, F. Baftizadeh, A. Budzillo, B. R. Lee, T. Jarsky, L. Alfiler, K. Baker, E. Barkan, K. Berry, et al. Integrated morphoelectric and transcriptomic classification of cortical gabaergic cells. *Cell*, 183(4):935–953, 2020.

15. M. He, J. Tucciarone, S. Lee, M. J. Nigro, Y. Kim, J. M. Levine, S. M. Kelly, I. Krugikov, P. Wu, Y. Chen, et al. Strategies and tools for combinatorial targeting of gabaergic neurons in mouse cerebral cortex. *Neuron*, 91(6):1228–1243, 2016.

16. M. Larkum. A cellular mechanism for cortical associations: an organizing principle for the cerebral cortex. *Trends in neurosciences*, 36(3):141–151, 2013.

17. J. Ledderose, T. A. Zolnik, M. Toumazou, T. Trimbuch, C. Rosenmund, B. J. Eickholt, D. Jaeger, M. E. Larkum, and R. Sachdev. Input to layer 1 of somatosensory cortex: Local input outweighs long-range and can modulate the activity of layer 1 interneurons. *bioRxiv*, 2021.

18. Y.-H. Liu and X.-J. Wang. Spike-frequency adaptation of a generalized leaky integrate-and-fire model neuron. *Journal of computational neuroscience*, 10(1):25–45, 2001.

19. R. R. Llinás. The intrinsic electrophysiological properties of mammalian neurons: insights into central nervous system function. *Science*, 242(4886):1654–1664, 1988.

20. K. C.-K. Malina, E. Tsivourakis, D. Kushinsky, D. Apelblat, S. Shtiglitz, E. Zohar, M. Sokoletsky, G.-i. Tasaka, A. Mizrahi, I. Lampl, et al. Ndnf interneurons in layer 1 gain-modulate whole cortical columns according to an animal's behavioral state. *Neuron*, 109(13):2150–2164, 2021.

21. H. Markram, M. Toledo-Rodriguez, Y. Wang, A. Gupta, G. Silberberg, and C. Wu. Interneurons of the neocortical inhibitory system. *Nature reviews neuroscience*, 5(10):793–807, 2004.

22. A. Prönneke, M. Witte, M. Möck, and J. F. Staiger. Neuromodulation leads to a burst-tonic switch in a subset of vip neurons in mouse primary somatosensory (barrel) cortex. *Cerebral Cortex*, 30(2):488–504, 2020.

23. J. Rinzel. A formal classification of bursting mechanisms in excitable systems. In *Mathematical topics in population biology, morphogenesis and neurosciences*, pages 267–281. Springer, 1987.

24. J. Rinzel and G. B. Ermentrout. Analysis of neural excitability and oscillations. *Methods in neuronal modeling*, 2:251–292, 1998.

25. F. Scala, D. Kobak, M. Bernabucci, Y. Bernaerts, C. R. Cadwell, J. R. Castro, L. Hartmanis, X. Jiang, S. Laturnus, E. Miranda, et al. Phenotypic variation of transcriptomic cell types in mouse motor cortex. *Nature*, 598(7879):144–150, 2021.

26. B. Schuman, S. Dellal, A. Prönneke, R. Machold, and B. Rudy. Neocortical layer 1: an elegant solution to top-down and bottom-up integration. *Annual Review of Neuroscience*, 44:221–252, 2021.

27. B. Schuman, R. P. Machold, Y. Hashikawa, J. Fuzik, G. J. Fishell, and B. Rudy. Four unique interneuron populations reside in neocortical layer 1. *Journal of Neuroscience*, 39(1):125–139, 2019.

28. G. Sciamanna and C. J. Wilson. The ionic mechanism of gamma resonance in rat striatal fast-spiking neurons. *Journal of neurophysiology*, 106(6):2936–2949, 2011.

29. J. N. Shin, G. Doron, and M. E. Larkum. Memories off the top of your head. *Science*, 374(6567):538–539, 2021.

30. G. D. Smith, C. L. Cox, S. M. Sherman, and J. Rinzel. Fourier analysis of sinusoidally driven thalamocortical relay neurons and a minimal integrate-and-fire-or-burst model. *Journal of neurophysiology*, 83(1):588–610, 2000.

31. K. M. Stiefel, B. Englitz, and T. J. Sejnowski. Origin of intrinsic irregular firing in cortical interneurons. *Proceedings of the National Academy of Sciences*, 110(19):7886–7891, 2013.

32. J. F. Storm. Temporal integration by a slowly inactivating k+ current in hippocampal neurons. *Nature*, 336(6197):379–381, 1988.

33. R. D. Traub and R. Miles. *Neuronal networks of the hippocampus*, volume 777. Cambridge University Press, 1991.

34. R. Tremblay, S. Lee, and B. Rudy. Gabaergic interneurons in the neocortex: from cellular properties to circuits. *Neuron*, 91(2):260–292, 2016.

35. X. Wang and J. Rinzel. Oscillatory and bursting properties of neurons, the handbook of brain theory and neural networks, m. arbib, ed, 1995.

36. X.-J. Wang. Ionic basis for intrinsic 40 hz neuronal oscillations. *Neuroreport*, 5(3):221–224, 1993.

37. X.-J. Wang, J. Tegnér, C. Constantinidis, and P. S. Goldman-Rakic. Division of labor among distinct subtypes of inhibitory neurons in a cortical microcircuit of working memory. *Proceedings of the National Academy of Sciences*, 101(5):1368–1373, 2004.

Acknowledgments

This work was supported by National Institutes of Health grants R01NS110079 to B.R. and X.W., and R01MH062349 to X.W. The authors thank Alvar Prönneke, Sean Froudist-Walsh, Kevin Berlemont and members of the Wang and Rudy labs for discussion.

Supplementary Materials

	Canopy n=27	NGFC n=21	$\alpha 7$ n=22	VIP n=13
Timescale (ms)	8.23 ± 1.72	9.53 ± 1.84	8.37 ± 3.86	18.34 ± 6.45
Resistance (MΩ)	133.5 ± 38.2	185.4 ± 50.4	135.3 ± 57.3	336.6 ± 83.0
Capacity (pF)	64.4 ± 14.0	53.3 ± 10.1	62.6 ± 12.5	45.1 ± 16.0
Delay (ms)	29.3 ± 15.1	497.9 ± 249.9	37.4 ± 17.4	113.8 ± 42.7
Rheobase (pA)	233.9 ± 70.1	$139.1.0 \pm 46.2$	212.6 ± 82.1	25.0 ± 25.6
fI Slope (Hz/pA)	1.04 ± 1.26	0.94 ± 1.19	0.25 ± 0.11	0.58 ± 0.32
IR width* (pA)	17.9 ± 25.3	/	91.8 ± 104.2	99.0 ± 121.9
AP Rise (mV/ms)	365.3 ± 83.8	419.7 ± 78.2	398.3 ± 99.9	480.1 ± 221.1
AP Decay (mV/ms)	-98.0 ± 23.9	-88.5 ± 19.8	-99.5 ± 29.3	-185.9 ± 67.7
AP Halfwidth (ms)	0.610 ± 0.107	0.657 ± 0.158	0.659 ± 0.189	0.456 ± 0.151
AP Reset (mV)	-50.0 ± 3.6	-52.9 ± 2.5	-47.8 ± 3.2	-52.8 ± 6.6
AP Threshold (mV)	-34.9 ± 3.0	-32.4 ± 1.7	-33.8 ± 2.3	-35.2 ± 4.9
AP max Volt (mV)	32.0 ± 6.4	35.6 ± 5.0	34.8 ± 5.8	38.9 ± 11.5

Table S1. Values are shown as mean $\pm$ SEM. Intrinsic electrophysiological properties of the four L1 interneurons subtypes. $*$: The IR width is only measured for the cells with an IR feature within each subtype (n=7, 9, 5 for Canopy, $\alpha 7$, and VIP cells, respectively). See method for details. The values are not exactly the same as the previous study ([27]) because we exclude the cells with fewer than 10 APs in the sweep with the maximum injection current.

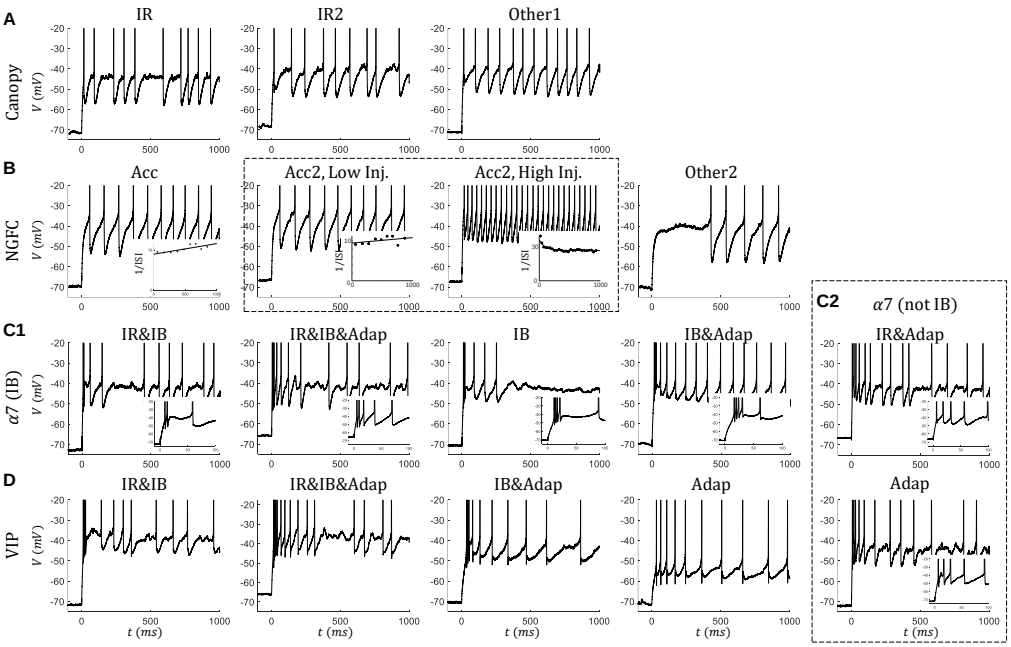

Figure S1. Examples that show different electrophysical features in four L1 interneuron subtypes. In (B), the two traces of Acc2 are from the same cell. The insets show the 1/ISI and the corresponding fitted line. Traces with about 10 APs are selected. In (C1, C2), the insets show the zoomed-in traces within the first 100ms. In (C2), the minimum initial firing rates of the corresponding $\alpha 7$ cells are $65.8Hz$ and $71.4Hz$, respectively.

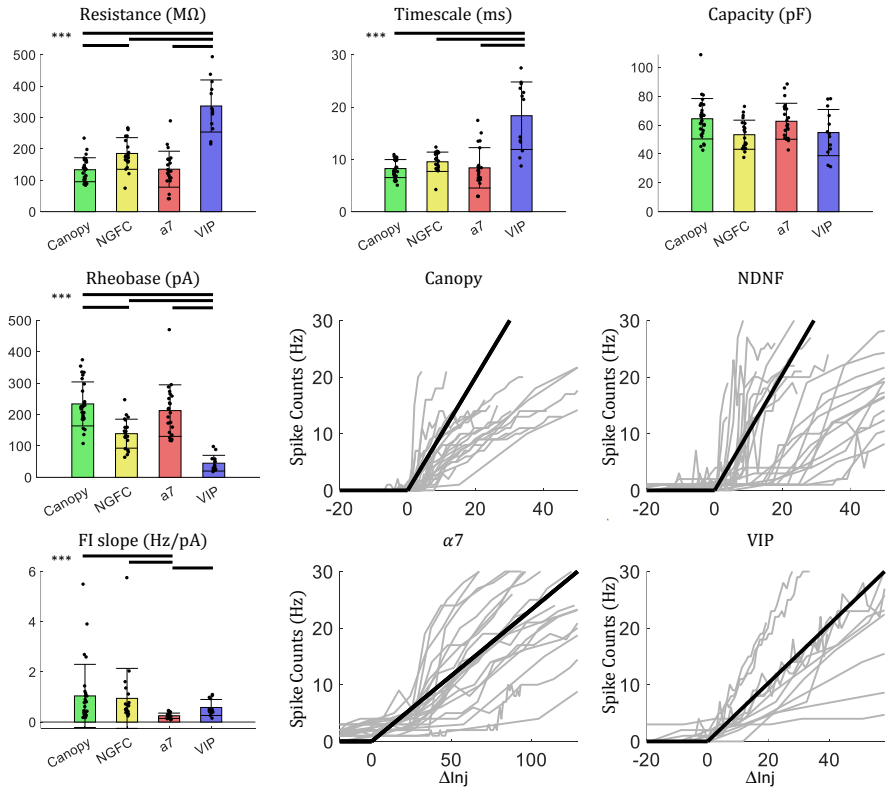

Figure S2. Electrophysiological features of the L1 interneurons. The bars above suggest the corresponding pair is significantly different ($p < 0.001$, Mann-Whitney U test). Rheobase and FI slope are measured by fitting the spike-count curve to a ReLU function. The bold black lines show the ReLU function with the mean FI slope. Grey lines represent individual spike-count curves of individual cells.

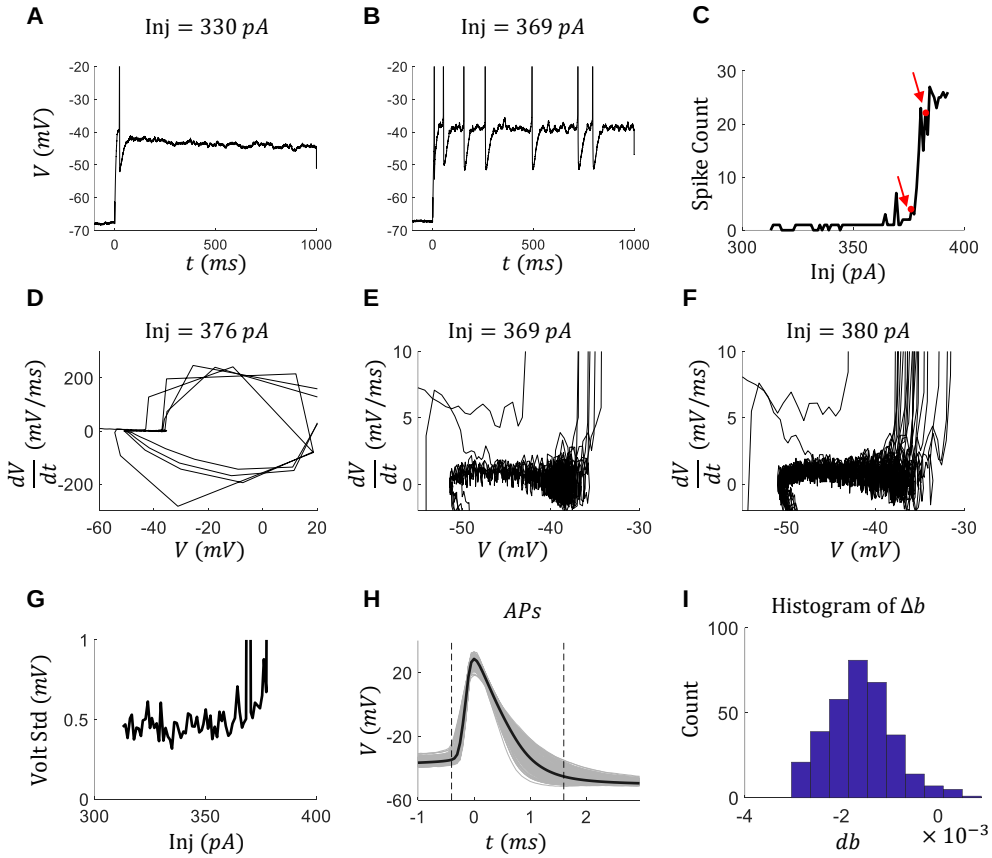

Figure S3. Further analyses on the data of the canopy cell. (A, B) More voltage traces of the same cell in Fig. 2 when Inj $= 330, 369pA$. Notice that the sweep with Inj $= 369pA$ has more APs than that with Inj $= 376pA$, reflecting the irregularity of the cell. (C) The spike counts over the $1s$ injection period. Red arrows indicate where Figure 2A, B locate. (D) The zoom-out phase diagram of Fig. 2D. (E, F) Phase diagrams of the cell when Inj $= 369, 380pA$, respectively. The window current around $-40mV$ is observed in both sweeps. (G) the voltage standard deviation measured between $500ms$ to $1s$ during the current injection. (H) The shapes of all the action potentials (AP) from all the sweeps of the same cell. We exclude the first two APs in every sweep. APs are aligned at the maximum of the voltage. The dashed lines indicate $t = -0.4, 1.6ms$, respectively. Voltage traces of these $2ms$ time windows are used to calculate the jump of the slow inactivation variable Δb. (I) The histogram of Δb when assuming $b_{init} = 0.28$ just before the AP. The value $b_{init} = 0.28$ is the average value after $3s$ of injection in the simulation. The average change is $< \Delta b >= -0.0020$.

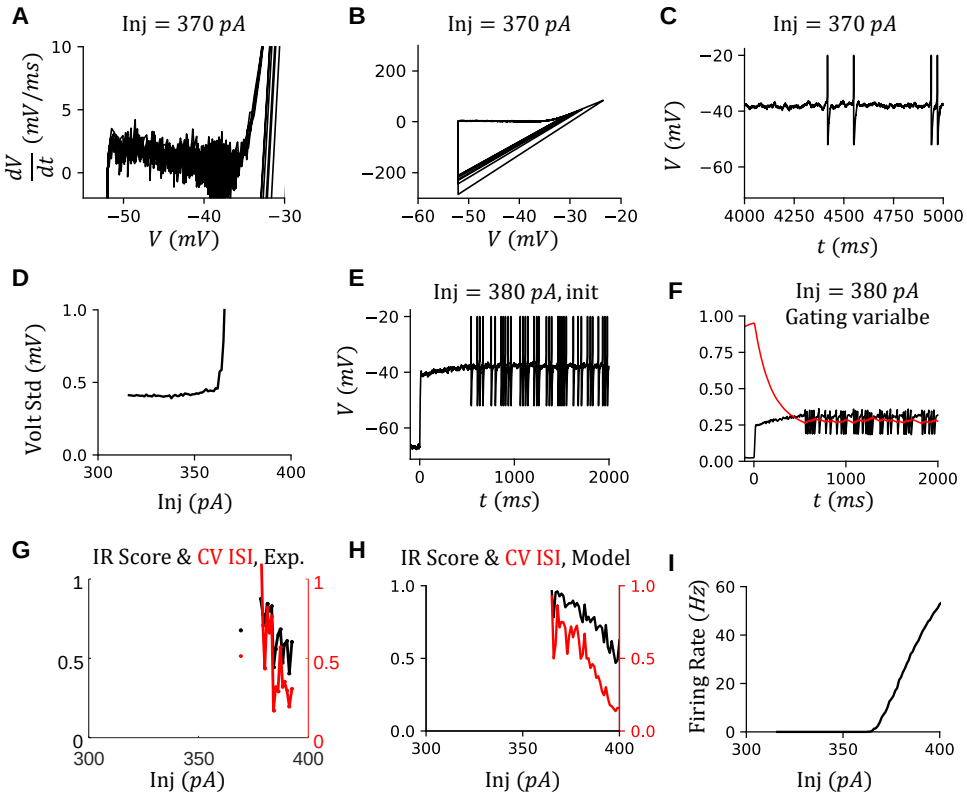

Figure S4. More results of the canopy cell model. (A) The phase diagram of the model when Inj $= 370pA$. (B) The zoom-out diagram of (A). (C) The voltage trace of the model when Inj $= 370pA$. (D) The voltage standard deviation in the model. (E) The voltage trace that includes the initial transient part when Inj$= 380pA$. (F) The transient dynamics of gating variables of SIK channel. The black and red lines indicate the fast and slow variable a and b, respectively. (G) The ISI ratio and CV ISI curves over injection currents in the experiment. (H) The ISI ratio and CV ISI curves of the model. (I) The f-I curve of the model.

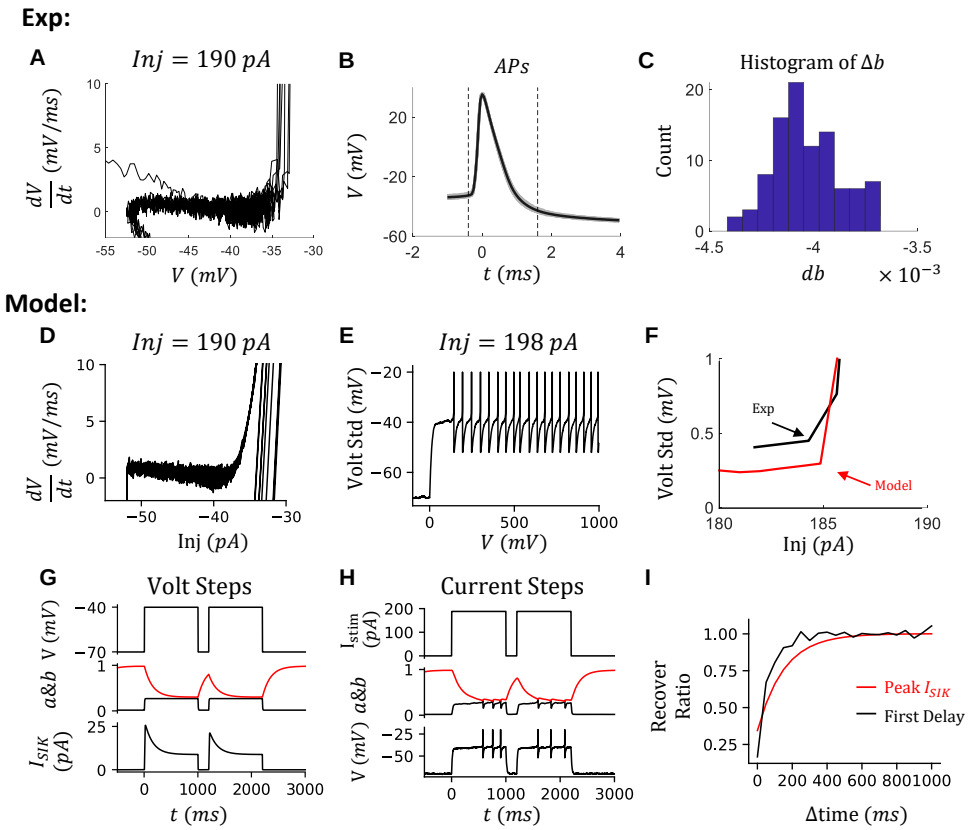

Figure S5. Further comparison between the experiment and the model of the NGFC. (A) The phase diagram of the cell when Inj $= 190pA$. (B) The shapes of all the APs of the same NGFC while excluding the first AP in every sweep. (C) The histogram of Δb assuming $b_{init} = 0.4$ before the AP. The average change is $< \Delta b >= -0.0040$. (D) Phase diagram of the model when Inj $= 190pA$. (E) The voltage trace of the model when Inj $= 198pA$. (F) The standard deviation of the voltage traces in the experiment (black) and the model (red) from $500ms$ to $1s$ during the current injection. (G) Simulation of the two voltage steps $V_{clamp} = -40mV$ with a resting time Δtime $= 200ms$. From top to bottom, voltage of the model, gating variables a (black) and b (red), SIK current I_{SIK}. (H) Simulation of the two current steps $I_{inj} = 188pA$ with a resting time Δtime $= 200ms$. From top to bottom, injection current, gating variables a (black) and b (red), voltage of the model. (I) The peak SIK current and delay of the first spike recover with a long resting time Δtime. The recover ratio of the peak SIK current (red) is calculated by comparing the maximum I_{SIK} during the second voltage step to that during the first voltage step. The delay of the 1st spike is calculated from the current steps (black).

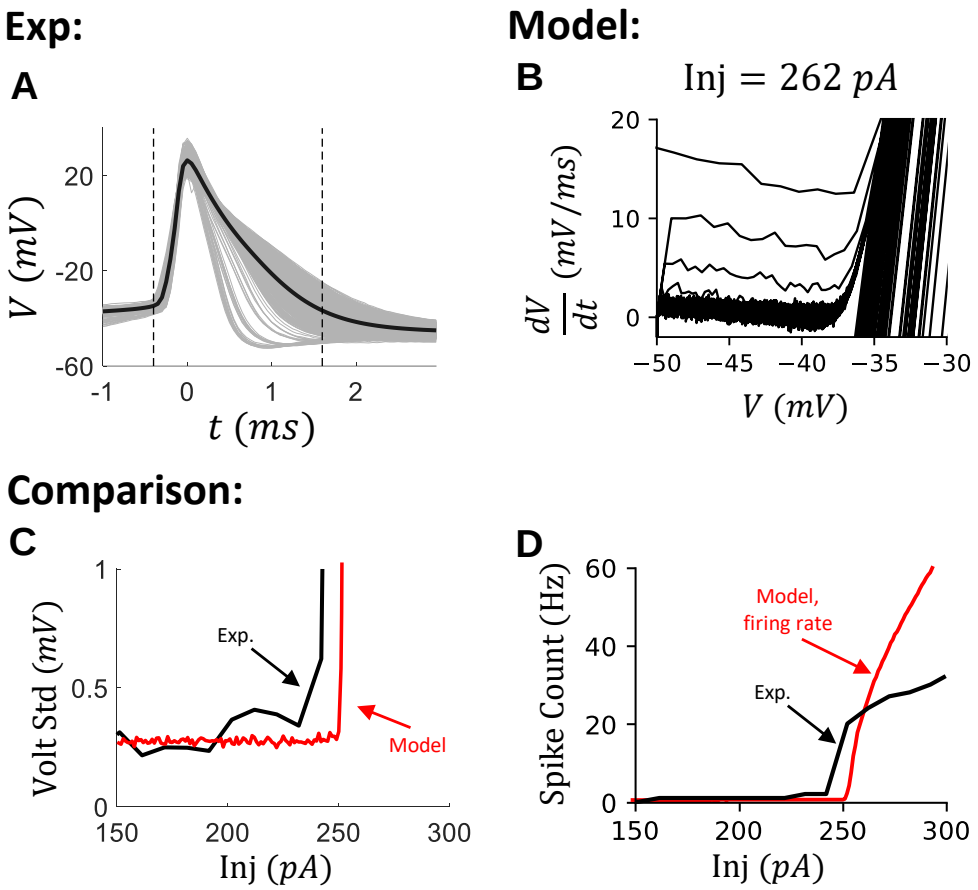

Figure S6. Further comparison between the experiment and the model of an $\alpha 7$ cell. (A) The shapes of all the APs of the same $\alpha 7$ cell while excluding the first two APs in every sweep. (B) The phase diagram when Inj= $262pA$ in the model. (C) The standard deviation of the voltage traces in the data (black) and the model (red). (D) The number of APs during the $1s$ injection period at different injection currents (black) and the steady firing rate in the model (red). Notice the low but non-zero spike count before $240pA$. For these sweeps, all the APs are triggered during the first $20ms$, i.e., the IB period.

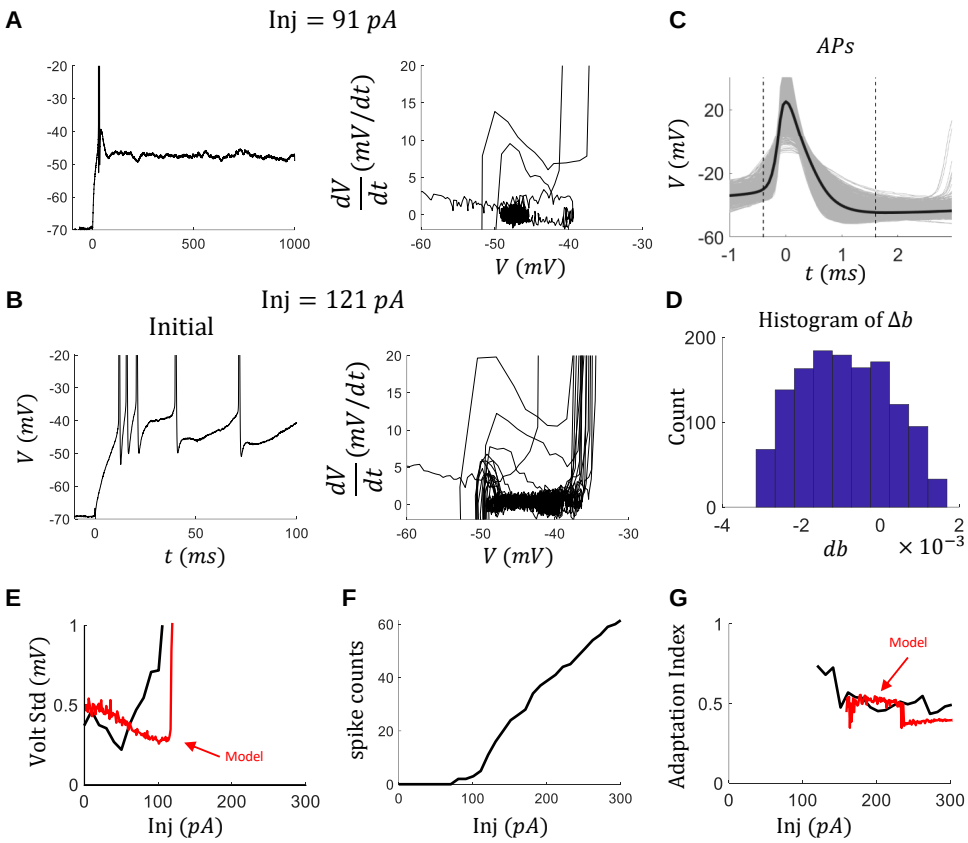

Figure S7. Further analyses on the data of the VIP cell. (A) The voltage trace over the $1s$ injection period (left) and phase diagram (right) when Inj= $91pA$. The firing stops after the IB period in this sweep. (B) The voltage trace over the first $100ms$ injection period (left) and phase diagram (right) when Inj= $121pA$. (C) All APs of the cell while excluding the first two APs in every sweep. (D) The histogram of Δb assuming $b_{init} = 0.25$ just before the AP. The average change is $< \Delta b >= -0.0009$. (E) The standard deviation of the voltage traces in the data (black) and the model (red). (F) The curve of spike counts during the $1s$ injection period. (G) The adaptation index (AI) from the data (black) and the model (red). AI is measured based on the fitting of 1/ISI from $100ms$ to $1s$.

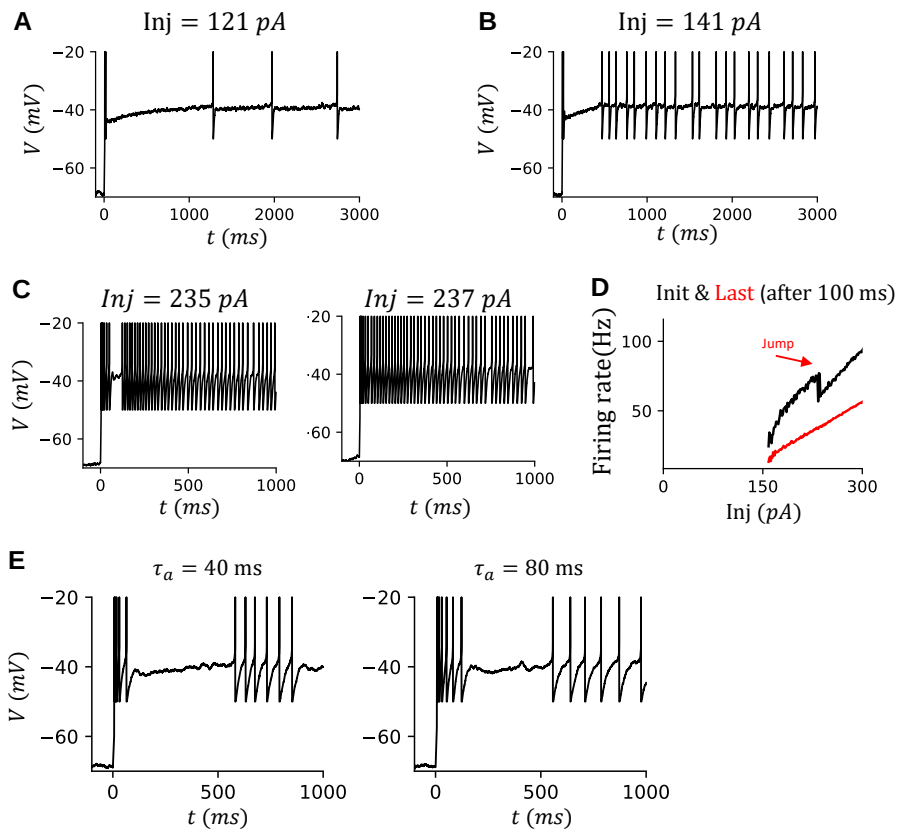

Figure S8. More results of the VIP cell model. (A, B) The voltage traces of the model in $3s$ at Inj $= 121, 141$. (C) The initial and last (steady-state) firing rates are measured from $100ms$ to $1500ms$. (D) The voltage traces of the model at Inj $= 235, 237pA$. The jump in the curve of the initial firing rate is due to the diminishing of the silent period after the initial bursting. The same reason leads to the jump in the AI curve (figure S7G). (E) Voltage traces when varying the time constant of fast activation variable $\tau_a = 40, 80ms$ when injection current Inj=$141pA$. The firing pattern around $100ms$ is more comparable between the data and the model. However, τ_a is not biologically plausible anymore (Original $\tau_a = 4ms$).

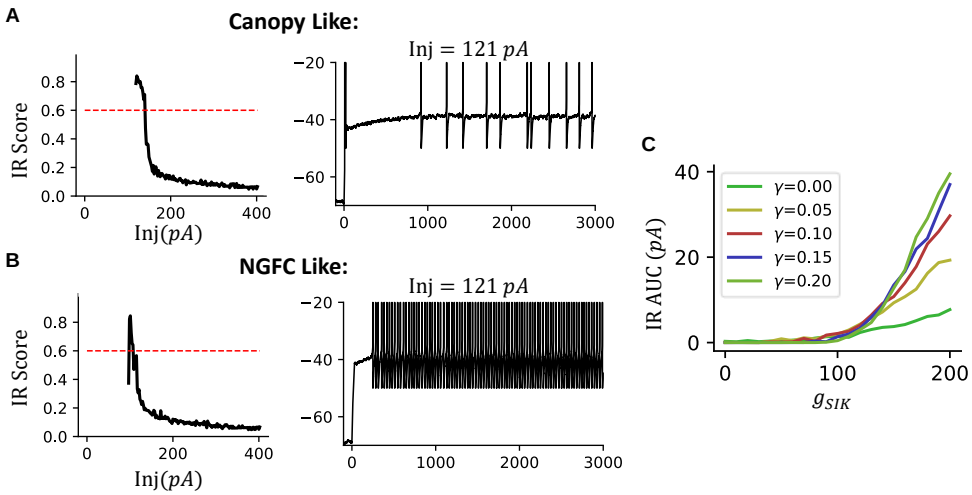

Figure S9. Model results when the parameters are in the Canopy-cell-like region and NGFC-like region. (A) The results of the model in Fig. 8 when set $\gamma = 0, g_{SIK} = 150nS$ looks like a canopy cell. (Left) The IR score. The drop of the curve is sharp when increasing the injection current, and the IR width is small. (Right) Voltage trace at Inj=121pA (B) The model results when setting $\gamma = 0, g_{SIK} = 90nS$ looks like an NGFC. The IR width is further reduced in comparison to (A). In this case, we remove the T-type Ca^{2+} current for better visualization. (C) Irregular area-under-curve (AUC) over different SIK conductance g_{SIK} and adaptation strength γ. The IR AUC is defined as the area under the curve of ISI ratio and above the threshold ISI ratio= 0.6 in Fig. 8C. The IR AUC starts saturating when the adaptation strength γ is big.

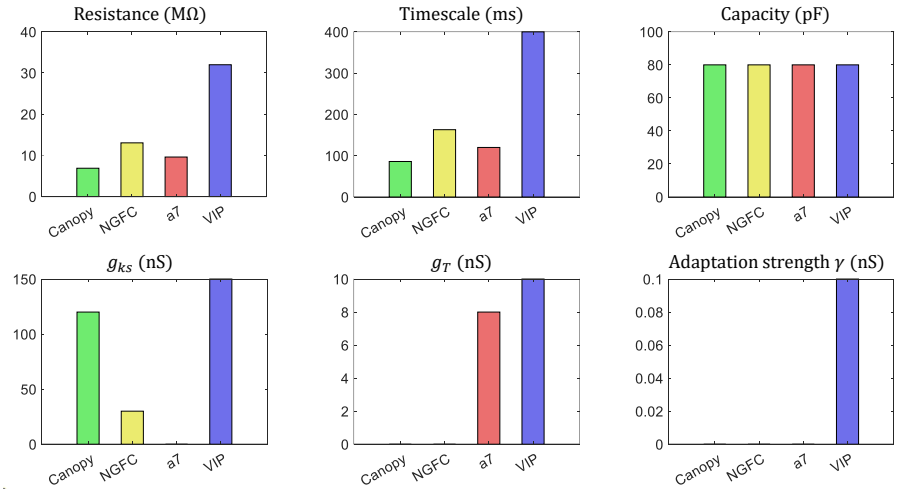

Figure S10. Bar plots of model parameters in this paper. See table 1 for detailed values.